International Journal of Heat and Mass Transfer 258 (2026) 128283

Contents lists available at ScienceDirect

International Journal of Heat and Mass Transfer

journal homepage: www.elsevier.com/locate/hmt

Interfacial and coherent thermal transport of phonons in Bi_2Te_3/Sb_2Te_3 superlattices

Bin Liu [a], Zhiguo Tian [a], Alexander A. Barinov [b], Moran Wang [a,*]

[a] Key Laboratory for Thermal Science and Power Engineering of Ministry of Education, Department of Engineering Mechanics, Tsinghua University, Beijing 100084, China

[b] Department of Thermophysics, Bauman Moscow State Technical University, Moscow 105005, Russia

ARTICLE INFO

Dataset link: https://github.com/binliu93/Data_for_Bi2Te3-Sb2Te3

Keywords:
Superlattice
Lattice thermal conductivity
Interfacial thermal conductance
Machine learning potential
Wave equation

ABSTRACT

Bi_2Te_3 and Sb_2Te_3, as typical layered chalcogenide semiconductors, exhibit excellent thermoelectric performance near room temperature. Engineering phonon transport through nanostructures has become an important strategy for optimizing thermoelectric material performance. This study employs neuroevolution potential combined with molecular dynamics simulations to systematically investigate the interfacial scattering and coherent (wavelike) transport mechanisms of phonons in Bi_2Te_3/Sb_2Te_3 superlattices. Based on density functional theory calculations, we constructed a dataset and trained a machine learning potential for Bi_2Te_3/Sb_2Te_3 heterostructures. The lattice thermal conductivity of superlattices was calculated using the homogeneous non-equilibrium molecular dynamics method, and the wavelike transport characteristics of phonons were analyzed from a wave mechanics perspective by combining phonon wave equations and transfer matrix methods. The study reveals that Bi_2Te_3/Sb_2Te_3 superlattices exhibit minimum lattice thermal conductivity at a period thickness of approximately 5 nm, with thermal conductivity showing non-monotonic variation with period thickness. Spectral thermal conductivity analysis demonstrates that this non-monotonic behavior represents a fundamental transition of phonons from coherent wavelike to incoherent particlelike transport. Phonon wave equation calculations further show that Bragg scattering conditions form phonon bandgaps at specific frequency-angle combinations, leading to selective phonon blockade. With systematic variation of period thickness, the position, number, and width of bandgaps exhibit clear evolutionary patterns. In short-period superlattices with fixed period thickness, increasing the number of interfaces can effectively enhance interference effects, making phonon forbidden bands more distinct and frequency selectivity stronger. This study provides theoretical insights into the microscopic mechanisms of phonon wavelike effects in superlattices and offers guidance for interface engineering and performance optimization of nanostructured thermoelectric materials.

1. Introduction

Thermoelectric materials enable direct conversion between thermal and electrical energy, offering significant potential for waste heat recovery and solid-state refrigeration applications [1]. Bi_2Te_3 and Sb_2Te_3, as representative layered chalcogenide semiconductors, exhibit low thermal conductivity perpendicular to the layer interfaces owing to their distinctive quintuple-layer (Te–Bi/Sb–Te–Bi/Sb–Te) crystal structure, positioning them among the most promising thermoelectric materials for near-room-temperature applications [2]. In recent years, engineering phonon transport through alloying and nanoheterostructure fabrication to reduce lattice thermal conductivity (LTC) has emerged as a critical strategy for thermoelectric performance enhancement [3,4]. $Bi_xSb_{2-x}Te_3$ solid-solution alloys effectively suppress phonon propagation via mass-difference scattering and alloy disorder scattering between Bi and Sb atoms [5–7]. Concurrently, Bi_2Te_3/Sb_2Te_3 nanoheterostructures exploit interface scattering and energy carrier filtering mechanisms that diminish LTC while simultaneously enhancing the Seebeck coefficient, thus enabling synergistic optimization of thermoelectric properties [8–15].

Ju et al. demonstrated that Bi_2Te_3/Sb_2Te_3 interface engineering effectively reduces LTC in their core–shell heterojunction nanoplates [11]. Their investigation revealed that increasing Sb_2Te_3 shell thickness correspondingly increased the density of heterojunction interfaces, resulting in enhanced phonon scattering and substantial reduction in LTC. The pronounced inhibition of phonon transport by interface scattering

* Corresponding author.
E-mail address: mrwang@tsinghua.edu.cn (M. Wang).

https://doi.org/10.1016/j.ijheatmasstransfer.2025.128283
Received 29 September 2025; Received in revised form 23 November 2025; Accepted 16 December 2025
Available online 29 December 2025

manifested as markedly lower cross-plane LTC compared to the in-plane direction, enabling the Bi_2Te_3/Sb_2Te_3 sample to achieve a zT value of approximately 0.94 in the cross-plane direction at 500 K. Kimberly et al. established that interfaces between two-dimensional Sb_2Te_3 and Bi_2Te_3 nanoplates substantially enhance phonon scattering while dramatically reducing LTC in the perpendicular direction [12]. Concurrently, energy carrier filtering effects at these interfaces enabled the 15% Bi_2Te_3 composite to attain a Seebeck coefficient of 210 μV/K, culminating in a high zT value of approximately 1.26 at 450 K. These findings collectively underscore the pivotal role of engineered interfaces in suppressing LTC through enhanced phonon scattering mechanisms.

In pioneering research, Venkatasubramanian discovered that LTC in short-period Bi_2Te_3/Sb_2Te_3 superlattices (SLs) was substantially lower than in homogeneous solid-solution alloys [14]. At an optimal SL period of ~5 nm, the LTC reached a minimum of 0.22 W m^{-1} K^{-1}, representing a 2.2-fold reduction compared to solid-solution alloys of equivalent composition. This work introduced a physical model based on coherent backscattering of wavelike phonons at SL interfaces, proposing that low-frequency phonons undergo strong interfacial scattering, resulting in localization-like behavior that effectively suppresses low-frequency phonon thermal transport. This phonon localization mechanism provided crucial theoretical insights into LTC reduction in SL structures while establishing a foundation for subsequent research on phonon transport control through periodic nanostructures. Building on these fundamental insights, Venkatasubramanian et al. recently achieved a breakthrough in thermoelectric refrigeration using controlled hierarchically engineered superlattice structures [8]. Their p-type Bi_2Te_3/Sb_2Te_3 and n-type $Bi_2Te_3/Bi_2Te_{2.7}Se_{0.3}$ nano-engineered films exhibited zT values 100% higher than conventional Bi_2Te_3-based bulk materials near room temperature, attributed primarily to reduced LTC (~8 vs. 16 mW m^{-1} K^{-1}) at SL interfaces. The resulting solid-state refrigeration system demonstrated a 70% improvement in system-level zT over conventional bulk thermoelectric devices, achieving efficient refrigeration (1.2 W heat pumping) with minimal power consumption (80 mW).

These experimental advances collectively underscore the critical role of phonon interfacial scattering and wavelike transport phenomena in thermal conductivity suppression within Bi_2Te_3/Sb_2Te_3 nanoheterostructures. However, the underlying microscopic mechanisms governing phonon interfacial scattering, wavelike interference, and localization phenomena within Bi_2Te_3/Sb_2Te_3 nanoheterostructures remain incompletely understood. A comprehensive theoretical framework is essential to elucidate the fundamental physics behind these interfacial effects and provide predictive capabilities for rational interface design [16–18]. Chowdhury et al. employed non-equilibrium molecular dynamics (NEMD) simulations with developed Morse interatomic potentials to systematically investigate the thermal transport properties of Bi_2Te_3/Sb_2Te_3 interfaces and SLs, providing crucial computational insights into the phonon transport mechanisms in these materials [19]. The study comprehensively examined the LTC variation across SLs with different period thicknesses, reproducing the experimentally observed minimum LTC in Bi_2Te_3/Sb_2Te_3 systems. This minimum was attributed to the competing effects between incoherent and coherent phonon transport regimes. However, the inherent limitations of MD simulations in providing mode-resolved phonon analysis preclude detailed understanding of wavelike transport phenomena, including interface scattering, interference, and localization of coherent phonons within SLs. Furthermore, the predictive capability of MD simulations is highly dependent on the accuracy of interatomic potentials [20,21]. In recent years, machine learning potentials (MLPs) have emerged as a transformative computational tool that combines the high accuracy of first-principles methods with the computational efficiency of classical MD, enabling the exploration of complex materials systems with unprecedented precision while maintaining feasible computational costs for large-scale and long-timescale simulations. Zhang et al. developed a deep neural network potential to investigate the thermal transport properties of Sb_2Te_3 and Bi_2Te_3/Sb_2Te_3 SLs [22,23]. The study successfully predicted the LTC of Sb_2Te_3 and minimum LTC phenomenon in Bi_2Te_3/Sb_2Te_3 SLs, with results demonstrating good agreement with experimental values. The work also provided detailed insights into the underlying phonon physics through weighted phase space analysis and Grüneisen parameter calculations, including the identification of stronger anharmonicity in the cross-plane direction.

In this study, we employ the neuroevolution potential (NEP) model combined with large-scale MD simulations to systematically investigate phonon interfacial scattering and wavelike transport mechanisms in Bi_2Te_3/Sb_2Te_3 SLs [24]. NEP demonstrates superior computational performance compared to other MLP models, with computational speeds exceeding similar models by more than an order of magnitude [25,26]. This high computational efficiency enables sufficient statistical sampling for large-scale systems, thereby overcoming previous limitations in size and time scales that hindered detailed understanding of phonon transport mechanisms in complex heterostructures. This study first constructed a comprehensive training dataset for Bi_2Te_3/Sb_2Te_3 heterostructures based on density functional theory (DFT) calculations and trained the NEP model accordingly. The accuracy of the NEP model was validated by comparing the predicted LTC of Bi_2Te_3 and Sb_2Te_3, as well as interfacial thermal conductance (ITC), with published experimental data and theoretical results. Using the homogeneous non-equilibrium molecular dynamics (HNEMD) method, we systematically investigated the relationship between interface density and LTC in Bi_2Te_3/Sb_2Te_3 SLs. Furthermore, through spectral LTC decomposition, we quantified the frequency-dependent phonon contributions to heat conduction to gain a deeper understanding of the underlying phonon transport mechanisms. Combining phonon wave equations and mode analysis, we further studied the wavelike (or coherent) phonon transport characteristics in Bi_2Te_3/Sb_2Te_3 SLs. By analyzing phonon reflection, transmission, and coherent interference behavior at heterointerfaces, we elucidated the mechanisms by which interfacial scattering and wavelike effects govern from a wave dynamics perspective, providing a theoretical foundation for interpreting experimentally observed wavelike phonon phenomena.

2. Methodology

2.1. Density functional theory calculations and training dataset construction

In this work, DFT calculations were performed using projector augmented wave pseudopotentials and the Perdew–Burke–Ernzerhof generalized gradient approximation exchange–correlation functional [27,28]. For geometric optimization of Bi_2Te_3 and Sb_2Te_3 systems, the plane wave cutoff energy was set to 600 eV, with Brillouin zone sampling using a Γ-centered 15 × 15 × 2 k-point mesh. The energy convergence criterion for electronic self-consistent calculations was set to 1×10^{-10} eV, and the atomic force convergence criterion for structural optimization was 1×10^{-6} eV/Å. To accurately describe interlayer van der Waals interactions, DFT-D3 dispersion correction was incorporated in the calculations [29]. Spin–orbit coupling (SOC) was not included in the present DFT calculations. Although Bi and Sb are heavy elements where SOC can significantly affect electronic band structures, previous studies have demonstrated that non-SOC DFT calculations with appropriate van der Waals corrections can accurately reproduce phonon dispersion relations and predict LTC values in good agreement with experiments for both Bi_2Te_3 and Sb_2Te_3 [23,30,31]. Phonon density of states (DOS) and group velocities were calculated using the PHONOPY package combined with the finite displacement method [32,33], where harmonic force constant matrices were obtained from a 4 × 4 × 1 supercell structure and a 2 × 2 × 1 k-point mesh.

The training dataset encompassed pure-phase Bi_2Te_3 and Sb_2Te_3, Bi_2Te_3/Sb_2Te_3 heterointerface structures, as well as atomic randomly distributed configurations of $Bi_xSb_{2-x}Te_3$ alloy. Initial structural configurations were generated through MD simulations combined with the

Table 1
Composition of the NEP training dataset for Bi_2Te_3/Sb_2Te_3 heterostructures.

Configuration type	Count	Percentage (%)	Atoms per configuration
Bi_2Te_3	677	32.6	240
Sb_2Te_3	600	28.9	240
Bi_2Te_3/Sb_2Te_3 interface & $Bi_xSb_{2-x}Te_3$ alloy	800	38.5	240–304
Total	2077	100	–

NEP89 universal MLP [34,35]. This potential can handle 89 chemical elements and complex heterointerface interactions, offering significant computational efficiency advantages compared to traditional ab initio molecular dynamics (AIMD) methods. Specifically, representative structures of various types were first equilibrated under zero pressure using NPT ensemble for 0.5 ns in the temperature range of 50–600 K, followed by 4 ns NVT ensemble sampling, with representative configurations extracted from the entire simulation trajectory at 0.1 ns intervals. To further enhance structural diversity, uniformly distributed random strains ranging from −3% to +3% were applied to selected extracted configurations, while Gaussian distributed noise perturbations with a standard deviation of 0.1 Å were added to atomic coordinates [36]. Total energies, atomic forces, and virial tensors for all training structures were obtained through DFT static single-point calculations. Considering the balance between computational accuracy and efficiency, single-point calculations employed a plane wave cutoff energy of 400 eV, with an electronic self-consistent convergence criterion of 1×10^{-6} eV. Due to the size of training structures being greater than or equal to 240 atoms, Brillouin zone sampling was performed using a Γ-centered $1 \times 1 \times 1$ k-point mesh. To ensure the completeness and representativeness of the training dataset, an iterative dataset construction strategy was employed. In each iteration, the current NEP model was used to predict candidate structures, with priority given to selecting structures with large prediction errors or located at the boundaries of descriptor space for DFT single-point calculations to obtain reference data, followed by incorporating the newly obtained data into the training dataset and updating the model. During the model updating process, the fine-tuning functionality of the NEP architecture was utilized, performing incremental learning based on model parameters obtained from NEP89 to derive the NEP model for the current iteration, rather than training from scratch [34]. This approach significantly improves training efficiency by maintaining descriptor normalization parameters and reusing the mean and variance parameters from the separable natural evolution strategy. Through multiple rounds of MD simulations, intelligent structure sampling, and DFT calculations in a cyclical process, the training dataset was progressively expanded to cover a broader configurational space, ensuring good predictive capability of the model within the target temperature and pressure ranges.

The finally constructed training dataset contains a total of 2077 atomic configurations, distributed across four categories as summarized in Table 1.

2.2. Training of neuroevolution potential model

With the aforementioned training dataset, we trained a MLP based on the NEP model to describe the interatomic interactions in Bi_2Te_3/Sb_2Te_3 heterostructures. The NEP framework combines a neural network architecture for representing the potential energy surface with the separable natural evolution strategies optimization algorithm for model training. In the NEP training based on the DFT dataset, the cutoff radii for the radial and angular descriptor components were set to 8 Å and 5 Å, respectively, to effectively capture the interlayer van der Waals interactions in the layered structures of Bi_2Te_3 and Sb_2Te_3 [30,31,37]. The accuracy of the constructed NEP model was validated through comparison with DFT reference calculations, as shown in Fig. 1. The parity plots demonstrate good agreement between NEP predictions and DFT calculations across all evaluated properties, with root mean square errors (RMSE) of 1.9 meV/atom for energy, 93 meV/Å for atomic forces, and 19 meV/atom for virial. Comparison of phonon dispersion relations between the NEP model and DFT calculations demonstrates good agreement for acoustic phonon branches, with some deviations in high-frequency optical modes that have minimal impact on LTC predictions (see Supporting Information, Section 1). The accuracy of the NEP model in predicting thermal transport properties was further validated through subsequent calculations of LTC for Bi_2Te_3 and Sb_2Te_3 and their ITC.

2.3. Homogeneous nonequilibrium molecular dynamics and spectral thermal conductivity decomposition

The HNEMD method with the trained NEP model was employed to calculate the LTC of pure-phase Bi_2Te_3 and Sb_2Te_3, as well as Bi_2Te_3/Sb_2Te_3 SLs [38]. All HNEMD simulations were conducted using the GPUMD software package [35]. In this approach, thermal transport is simulated by applying an external driving force $\mathbf{F}_i^{ext}$ on each atom i according to the generalized Evans method:

$$\mathbf{F}_i^{ext} = E_i \mathbf{F}_e + \mathbf{F}_e \cdot \mathbf{W}_i, \tag{1}$$

where $\mathbf{F}_e$ represents the driving force parameter with dimensions of inverse length, E_i denotes the total energy of atom i, and $\mathbf{W}_i$ is the per-atom virial tensor. This external perturbation drives the system away from equilibrium, inducing a non-equilibrium heat current $\langle \mathbf{J} \rangle_{ne}$ that exhibits a linear relationship with $\mathbf{F}_e$ within the linear response regime:

$$\frac{\langle J^\mu(t) \rangle_{ne}}{TV} = \sum_\nu \kappa^{\mu\nu} F_e^\nu, \tag{2}$$

where $\kappa^{\mu\nu}$ represents the thermal conductivity tensor components, T is the system temperature, and V denotes the system volume.

Within the HNEMD framework, spectral decomposition of thermal conductivity can be performed to enable frequency-resolved analysis of phonon contributions to heat transport [39]. This decomposition is achieved through the calculation of the virial-velocity time correlation function:

$$\mathbf{K}(t) = \sum_i \langle \mathbf{W}_i(0) \cdot \mathbf{v}_i(t) \rangle, \tag{3}$$

where $\mathbf{W}_i(0)$ represents the virial tensor of atom i at time zero, $\mathbf{v}_i(t)$ is the velocity vector of atom i at time t, and the angular brackets denote ensemble averaging over multiple trajectories. The frequency-dependent thermal conductivity is subsequently obtained via Fourier transformation [38]:

$$\kappa(\omega) = \frac{2}{VTF_e} \int_{-\infty}^{\infty} e^{i\omega t} \mathbf{K}(t) dt, \tag{4}$$

with the total thermal conductivity recovered through frequency integration:

$$\kappa = \int_0^{\infty} \frac{d\omega}{2\pi} \kappa(\omega), \tag{5}$$

where V is the volume of the considered system and $K(t)$ represents the virial-velocity correlation function projected along the heat transport direction. This spectral analysis provides detailed insights into the frequency-dependent phonon transport mechanisms and enables identification of specific frequency ranges that dominate heat conduction in the investigated systems.

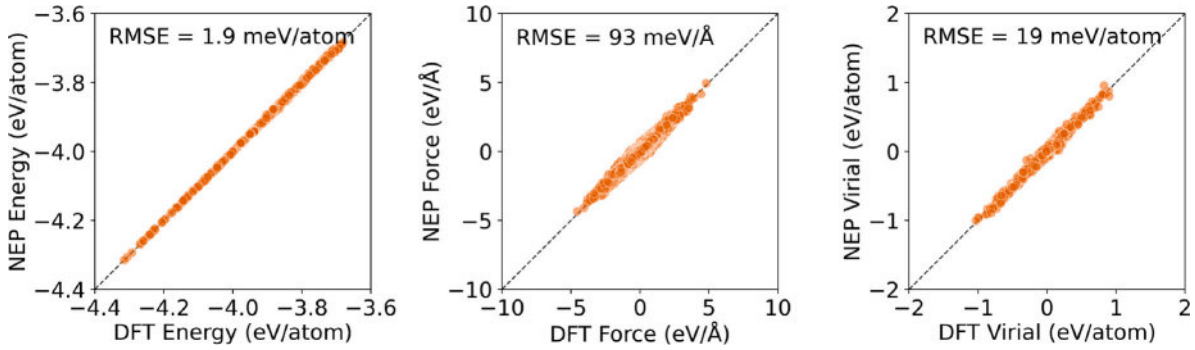

Fig. 1. Parity plots comparing NEP model predictions with DFT reference data for energy, forces, and virial.

2.4. Phonon wave equation and transfer matrix method

MD simulations, based on Newton's second law, study the dynamic behavior of materials through precise descriptions of interatomic potential [40]. For a system containing N atoms, the potential can be expanded in a Taylor series around equilibrium positions:

$$V\left(\mathbf{r}_1,\mathbf{r}_2,\ldots,\mathbf{r}_N\right)=V_0+\sum_{i=1}^{N}\sum_{\alpha}\frac{\partial V}{\partial r_{i\alpha}}u_{i\alpha}+\frac{1}{2!}\sum_{i,j=1}^{N}\sum_{\alpha,\beta}\frac{\partial^2 V}{\partial r_{i\alpha}\partial r_{j\beta}}u_{i\alpha}u_{j\beta}+\frac{1}{3!}\sum_{i,j,k=1}^{N}\sum_{\alpha,\beta,\gamma}\frac{\partial^3 V}{\partial r_{i\alpha}\partial r_{j\beta}\partial r_{k\gamma}}u_{i\alpha}u_{j\beta}u_{k\gamma}+\cdots, \tag{6}$$

where $u_{i\alpha}$ represents the displacement of the ith atom in the α direction relative to the equilibrium position, and α, β, γ denote the x, y, z directions in the Cartesian coordinate system. The terms in the potential expansion include harmonic (second-order term) and anharmonic (third-order and higher-order terms) interactions. By retaining all interaction terms in the potential expansion, MD simulations can completely describe the dynamic processes at the atomic scale, thereby naturally incorporating various phonon transport mechanisms (e.g., coherent and incoherent transport) [41–45].

Although MD simulations contain complete information about interactions at all orders and capture complex transport phenomena, they typically cannot provide mode-resolved insights into phonon transport. To deeply analyze the wavelike transport mechanisms of phonons in SLs, particularly the interfacial reflection, transmission, and interference phenomena, theoretical methods capable of providing mode-resolved analysis can be combined [46–48]. When the system exhibits small-amplitude vibrations, the harmonic approximation is applicable, retaining only the second-order term in the potential expansion. The harmonic approximation is mainly applicable to describing coherent phonon transport, while the anharmonic terms in MD simulations can capture incoherent processes such as phonon–phonon and interfacial diffuse scattering [49]. Under the harmonic approximation, the force on atom i in the α direction is:

$$F_{i\alpha}=-\frac{\partial V}{\partial u_{i\alpha}}=-\sum_{j,\beta}\boldsymbol{\Phi}_{i\alpha,j\beta}u_{j\beta}, \tag{7}$$

where $\boldsymbol{\Phi}_{i\alpha,j\beta}=\frac{\partial^2 V}{\partial r_{i\alpha}\partial r_{j\beta}}$ represents the harmonic force constant matrix elements. Combined with Newton's second law $m_i\frac{\partial^2 u_{i\alpha}}{\partial t^2}=F_{i\alpha}$, the harmonic lattice dynamics equation is obtained:

$$m_i\frac{\partial^2 u_{i\alpha}}{\partial t^2}=-\sum_{j,\beta}\boldsymbol{\Phi}_{i\alpha,j\beta}u_{j\beta}. \tag{8}$$

For periodic lattice structures, the above atomic-scale equation of motion can be transformed into a wave equation in the continuum mechanics framework through Fourier transformation. Assuming the displacement field has the form of a plane wave solution $u_{i\alpha}=\frac{1}{\sqrt{m_i}}\varepsilon_\alpha(\mathbf{k},s)e^{i(\mathbf{k}\cdot\mathbf{r}_i-\omega t)}$, where $\mathbf{k}$ is the wave vector, ω is the angular frequency, and $\varepsilon_\alpha(\mathbf{k},s)$ is the polarization vector of the sth phonon branch. In the long-wavelength limit ($|\mathbf{k}|\to 0$), the dispersion relation of acoustic phonon branches can be described by elastic continuum theory. Under the continuum approximation, the lattice displacement field $\mathbf{u}(\mathbf{r},t)$ satisfies the elastic wave equation:

$$\rho\frac{\partial^2\mathbf{u}}{\partial t^2}=(\lambda+2\mu)\nabla(\nabla\cdot\mathbf{u})-\mu\nabla\times(\nabla\times\mathbf{u}), \tag{9}$$

where ρ is the material density, and λ and μ are the Lamé elastic constants, related to the bulk modulus and shear modulus, respectively. This equation can be further decomposed into independent equations describing the propagation of pressure (P) and shear (S) waves, with phase velocities of $v_P=\sqrt{(\lambda+2\mu)/\rho}$ and $v_S=\sqrt{\mu/\rho}$, respectively. This theoretical framework provides a physical foundation for analyzing wavelike transport phenomena of phonons in multilayer heterostructures, such as interference and localization.

Based on the elastic wave equation, phonon propagation in multilayer heterostructures can be systematically analyzed using the transfer matrix method [50,51]. The fundamental principle of the transfer matrix method is to decompose complex multilayer heterostructures into wave propagation within individual layers and boundary condition treatment at interfaces, achieving calculation of overall transmission characteristics via the transfer matrix formalism [52]. Within each homogeneous layer, elastic wave propagation can be described by three basic modes: shear horizontal waves (SH waves), shear vertical waves (SV waves), and pressure waves (P waves), as shown in Fig. 2 [53,54]. For a given frequency ω and wave vector k, the displacement field of each wave mode in the nth layer can be expressed as a superposition of plane wave solutions. For SH waves, the displacement field in the nth layer is:

$$U_{j,n}(z)=A_{j,n}e^{ik_{j,n}z}+B_{j,n}e^{-ik_{j,n}z}, \tag{10}$$

where $j=tS$ or rS denotes the wave mode, the first letter represents the excited wave and the second letter represents its polarization, $A_{j,n}$ and $B_{j,n}$ are the amplitudes of forward propagating and backward reflected waves, respectively, $k_{j,n}=\omega/v_{j,n}$ is the wave number of the corresponding wave mode in that layer, and $v_{j,n}$ is the corresponding phase velocity. For the coupled case of SV and P waves, four wave amplitude components need to be considered simultaneously due to mode conversion at interfaces.

At interface z_n, elastic waves must satisfy displacement and stress continuity boundary conditions, require that the displacement and stress components on both sides of the interface are equal:

$$U_n(z_n)=U_{n+1}(z_n),\quad \sigma_n(z_n)=\sigma_{n+1}(z_n), \tag{11}$$

where the stress components are determined by elastic constants and displacement gradients. The amplitudes of transmitted and reflected resultant SH waves in the nth multilayer corresponding waves in the incident layer ($n=2N+2$), and substrate ($n=1$) are expressed as column vectors

$$\mathbf{w}_n=\begin{bmatrix}A_{tS,n}\\A_{rS,n}\end{bmatrix},\quad \mathbf{w}_{2N+2}=\begin{bmatrix}A_{iS,2N+2}\\A_{rS,2N+2}\end{bmatrix},\quad \mathbf{w}_1=\begin{bmatrix}A_{tS,1}\\0\end{bmatrix}. \tag{12}$$

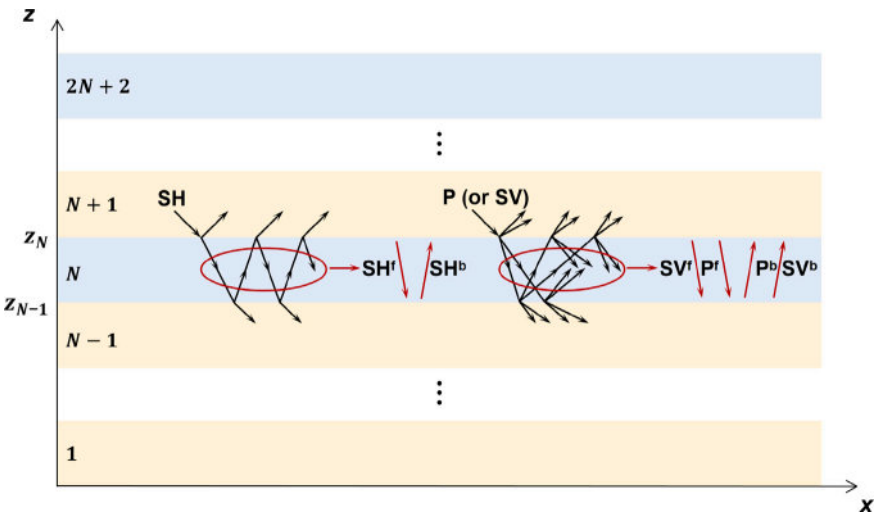

Fig. 2. Wavelike phonon reflection and transmission in the multilayer heterostructure. Superscripts f and b denote forward- and backward-propagating waves, respectively. Interface positions are marked as z_n, where n represents the layer index.

For shear waves, the stress is $\sigma_{j,n}(z) = \mu_n \partial U_{j,n}/\partial z$; for pressure waves, the stress is $\sigma_{j,n}(z) = (\lambda_n + 2\mu_n)\partial U_{j,n}/\partial z$. By applying boundary conditions, relationships between wave amplitudes in adjacent layers can be established. For SH waves, the transfer matrix $\mathbf{H}_n(z)$ is defined as:

$$\mathbf{H}_n(z) = \begin{bmatrix} e^{izk_{tS,n}\cos\theta_{tS,n}} & e^{-izk_{rS,n}\cos\theta_{rS,n}} \\ \mu_n k_{tS,n}\cos\theta_{tS,n} e^{izk_{tS,n}\cos\theta_{tS,n}} & -\mu_n k_{rS,n}\cos\theta_{rS,n} e^{-izk_{rS,n}\cos\theta_{rS,n}} \end{bmatrix}, \quad (13)$$

where $\theta_{tS,n}$ is the propagation angle of the SH wave in the nth layer, determined by Snell's law: $k_{\parallel} = k_{j,n}\sin\theta_{j,n} = \text{constant}$.

For SL structures containing N periods, the total transfer matrix $\mathbf{T}$ is obtained through multiplication of the transfer matrices of each layer:

$$\mathbf{T} = \mathbf{H}_1(z_1)^{-1}\mathbf{H}_2(z_2)\mathbf{H}_2(z_2)^{-1}\mathbf{H}_3(z_3)\cdots\mathbf{H}_{2N+1}(z_{2N+1})^{-1}\mathbf{H}_{2N+2}\left(z_{2N+2}\right). \quad (14)$$

By solving the transfer matrix equation $\mathbf{w}_1 = \mathbf{T}\mathbf{w}_{2N+2}$, the amplitude ratios of transmitted and reflected waves to the incident wave can be obtained. The phonon energy transmission coefficient α_j is defined as the ratio of transmitted energy flux $\eta_{j,1}$ to incident energy flux $\eta_{j,2N+2}$. For SH waves, the transmission coefficient is:

$$\alpha_{SH} = \frac{\eta_{tS,1}}{\eta_{iS,2N+2}} = \frac{\rho_1 v_{g,S,1}\cos\theta_{tS,1}}{\rho_{2N+2} v_{g,S,2N+2}\cos\theta_{iS,2N+2}}\left|\frac{A_{tS,1}}{A_{iS,2N+2}}\right|^2, \quad (15)$$

where $v_{g,j,n}$ is the group velocity and ρ_n is the density of the nth layer. For the coupled case of SV and P waves, the transmission coefficient needs to consider contributions from two polarization modes [47]. The group and phase velocities used in the transfer matrix calculations are determined by the phonon dispersion relations, $v_g(\omega) = \frac{\partial\omega}{\partial k}$ and $v_p(\omega) = \frac{\omega}{k}$. Therefore, the transmission coefficient is dependent on phonon polarization, frequency, and incident angle.

The phonon energy transmission coefficient is a key parameter characterizing the transport properties of phonons through multilayer heterostructures. According to the Landauer transport framework, the phonon transmission coefficient is a bridge connecting microscopic behavior and macroscopic thermal transport properties [55].

3. Results and discussion

3.1. Lattice thermal conductivity of pristine Bi_2Te_3 and Sb_2Te_3

To validate the accuracy and reliability of the trained NEP model for Bi_2Te_3/Sb_2Te_3 heterostructures, we first calculated the in-plane and cross-plane LTC of bulk Bi_2Te_3 and Sb_2Te_3 using the HNEMD method [38]. Both Bi_2Te_3 and Sb_2Te_3 are typical representatives of layered chalcogenide structures, featuring similar quintuple layer lattice configurations. Each quintuple layer can be represented as a Te_1–X–Te_2–X–Te_1 stacking sequence, where X represents Bi or Sb atoms. The key structural characteristic lies in the distinct bonding environments of the two types of Te atoms: Te_2 atoms form stable intralayer structures through strong covalent bonds with metal atoms, while Te_1 atoms maintain interlayer connections primarily through weaker van der Waals interactions. This bonding difference is the fundamental cause of their significant anisotropic thermal transport properties.

In the HNEMD calculations, to ensure the system remained within the linear response regime, we systematically tested the effect of different F_e values on LTC and ultimately determined the driving force parameters to be 1×10^{-4} Å^{-1} and 5×10^{-5} Å^{-1} for in-plane and cross-plane directions, respectively. These parameters are small enough to maintain linear response relationships while being large enough to achieve sufficient signal-to-noise ratio and statistical precision. The simulation system employed a 28 × 28 × 4 supercell configuration containing 47,040 atoms, with periodic boundary conditions applied in all x, y, and z directions to eliminate surface effects. System initialization included equilibration for 1 ns in the NPT ensemble at target temperature and zero pressure to ensure the structure reached thermodynamic equilibrium. Subsequently, during the data collection phase, a Nosé–Hoover chain thermostat was used to maintain the target temperature in the NVT ensemble, collecting 6 ns of heat flux data with a 1 fs time step to ensure adequate statistical sampling.

As shown in Fig. 3, the LTC results predicted by the MD-NEP method for Bi_2Te_3 and Sb_2Te_3 in the temperature range of 200–500 K demonstrate good agreement with reported experimental data and other theoretical calculations, validating the accuracy of the NEP model [23,30,56–60]. Both materials exhibit significant LTC anisotropy with values that are relatively close to each other. This is primarily attributed to their similar crystal structures, as well as their phonon DOS and group velocities, which we will compare in detail in the following sections.

3.2. Thermal transport properties of Bi_2Te_3/Sb_2Te_3 interfaces

Interfacial scattering plays a crucial role in both coherent interference and incoherent interfacial scattering of phonons in SLs [61–63]. To gain deep insight into the fundamental mechanisms affecting heat conduction at Bi_2Te_3/Sb_2Te_3 interfaces, we first systematically

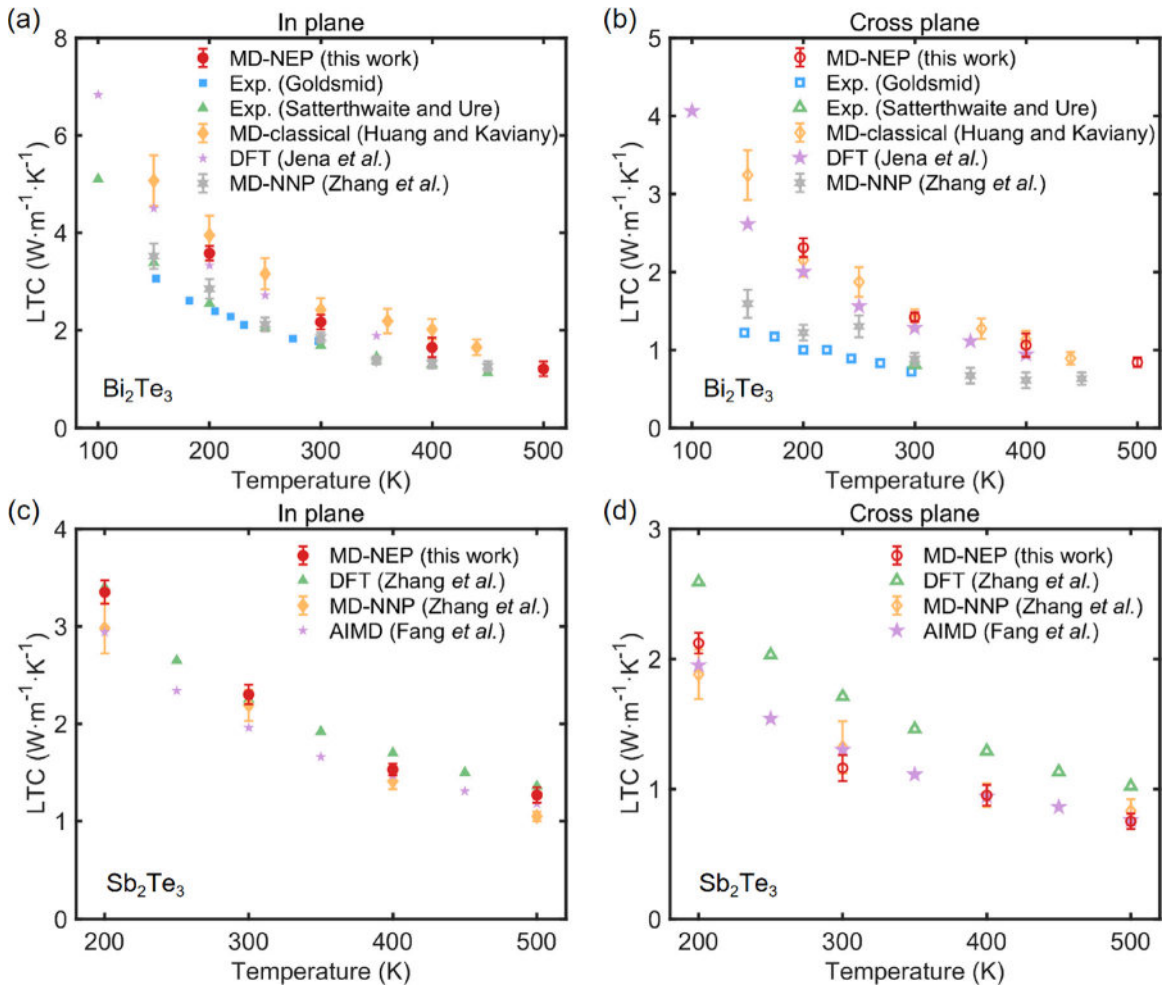

Fig. 3. Temperature-dependent in-plane and cross-plane LTC of Bi_2Te_3 and Sb_2Te_3 calculated using MD-NEP method (200–500 K), compared with experimental data and other computational approaches including DFT, MD simulations with classical potential (MD-classical) and neural network potential (MD-NNP) [23,30,56–60].

analyzed the intrinsic phonon property differences of the constituent materials based on DFT calculations. As shown in Fig. 4(a), the phonon DOS of Sb_2Te_3 extends toward higher frequency regions compared to Bi_2Te_3, primarily due to the significantly lighter mass of Sb atoms (121.76 u) compared to Bi atoms (208.98 u), resulting in an elevated phonon spectrum cutoff frequency. Sb_2Te_3 exhibits higher phonon mode density in the high frequency range (4–5 THz), providing more transport channels for heat conduction. Correspondingly, as shown in Fig. 4(b), the phonon group velocities of Sb_2Te_3 are generally higher than those of Bi_2Te_3 for most phonon branches. The difference in group velocities directly affects the phonon heat conduction capability and represents one of the primary microscopic origins of the LTC differences between the two materials [64].

These phonon property differences are not only reflected in the LTC performance of their respective bulk materials, but more importantly, according to phonon wave theory, when phonons propagate from one material to another, the mismatch in phonon spectrum and group velocities will produce complex elastic scattering phenomena at the interface, including phonon reflection, transmission, and total internal reflection processes under specific frequency and incident angle conditions. These interfacial scattering mechanisms will be analyzed in detail through phonon wave equations in subsequent sections.

To quantitatively evaluate the thermal transport performance of Bi_2Te_3/Sb_2Te_3 heterointerfaces, we constructed interface structures and performed NEMD simulations using NEP potentials. As shown in Fig. 4(c), the interface model consists of heterostructures composed of Bi_2Te_3(001) and Sb_2Te_3(001) crystal facets, ensuring good lattice matching and interface quality. To avoid boundary effects on heat conduction, the total system length is 54 nm, with an effective heat conduction measurement region of 42 nm. 3 nm fixed layers are set at both ends of the structure. The heat source and heat sink layers are each 3 nm thick, with temperature differences applied through the Langevin thermostat method. The cross-sectional area adopts a 15 × 15 unit cell configuration, corresponding to an effective cross-sectional area of 37.5 nm^2, ensuring statistical precision while maintaining reasonable computational cost.

NEMD simulations were performed using the GPUMD software package with a time step of 1 fs [35]. For each target temperature, a 4 ns structural relaxation process was first conducted, including NPT and NVT ensemble stages, to fully release interfacial stress and obtain thermodynamically equilibrated structures. Subsequently, with both ends of the system fixed, 10 ns NEMD runs were conducted with a constant temperature difference of ±30 K applied between the heat source and heat sink layers. To ensure the system reached a true non-equilibrium steady state, the first 5 ns of the production stage was used to establish a stable temperature gradient, while the steady-state data from the last 5 ns was used for ITC calculations. The interfacial temperature jump ΔT was precisely extracted through linear extrapolation: linear fitting was performed for the linear temperature distribution regions on both sides of Bi_2Te_3 and Sb_2Te_3 away from

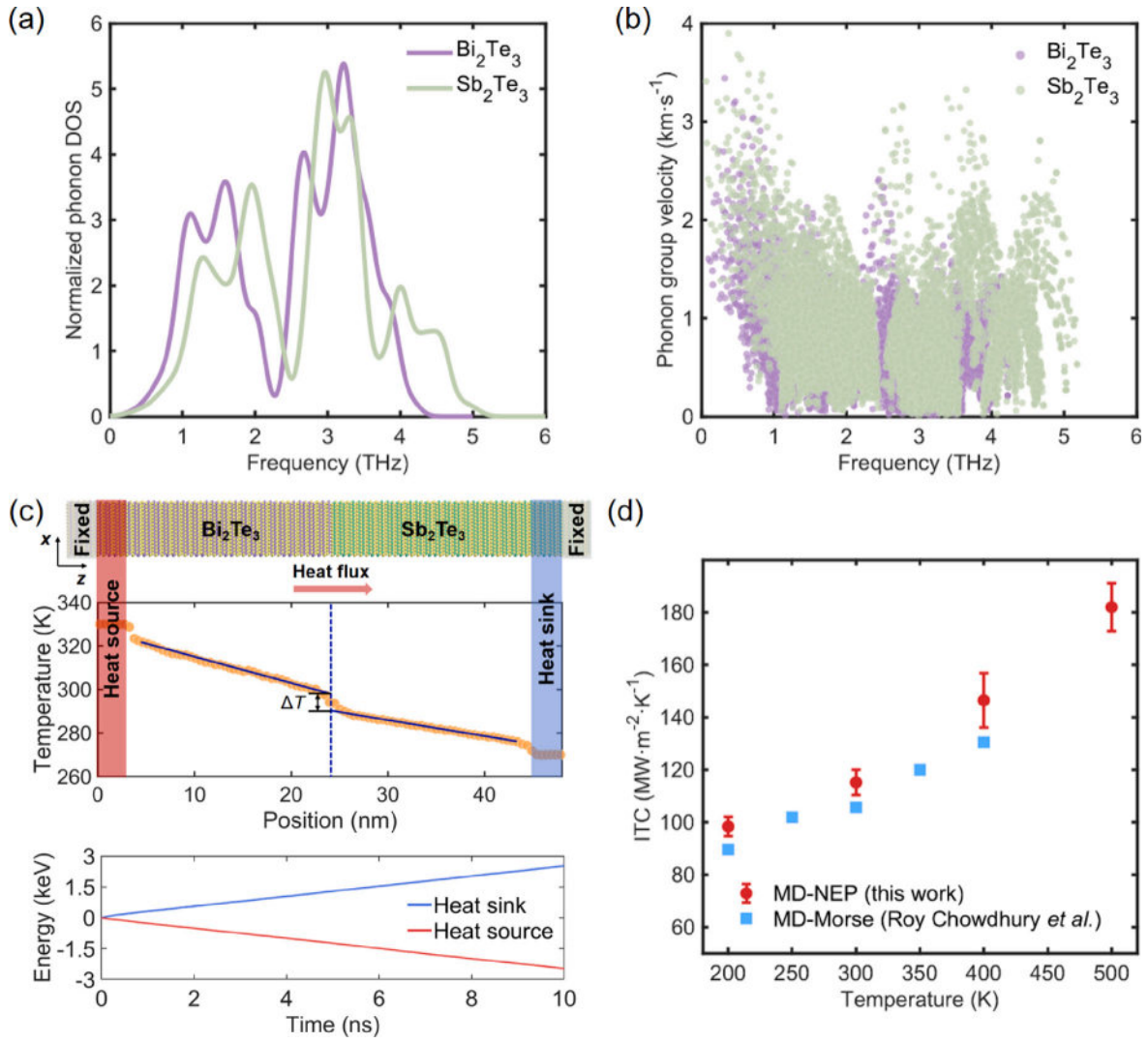

Fig. 4. (a) Normalized phonon DOS and (b) group velocity of Bi_2Te_3 and Sb_2Te_3 calculated using DFT. (c) Schematic diagram of ITC NEMD simulation setup (top), steady-state temperature distribution at 300 K (middle), and energy accumulation curves of heat source/sink (bottom), showing clear temperature jump (ΔT) at the interface. (d) Temperature-dependent ITC calculated using the MD-NEP method compared with MD-Morse potential results [19].

the interface, and the fitting lines were extrapolated to the interface midpoint position. The interfacial temperature difference was defined as the difference between the extrapolated temperatures on both sides. Finally, the ITC was calculated through the modified Fourier's law: $G = Q/(A \cdot \Delta T)$, where Q is the steady-state heat flux density and A is the interfacial cross-sectional area [65,66].

Fig. 4(d) shows the temperature-dependent ITC results calculated using the MD-NEP method, which demonstrate good agreement with MD-Morse potential calculation results [19,67,68]. Notably, the ITC increases significantly with rising temperature, indicating the important role of inelastic scattering processes in ITC at high temperatures. These results not only validate the reliability of the trained NEP model in predicting the thermal transport performance of Bi_2Te_3/Sb_2Te_3 heterointerfaces, but more importantly provide an important quantitative foundation for understanding the microscopic mechanisms of interfacial phonon scattering.

3.3. Minimum thermal conductivity in Bi_2Te_3/Sb_2Te_3 superlattices

To systematically investigate the transition of phonons from coherent to incoherent transport in Bi_2Te_3/Sb_2Te_3 SLs, we constructed a series of Bi_2Te_3(001)/Sb_2Te_3(001) SL structures having a constant total length of 120 nm and period thicknesses varying from 3.33 nm to 60 nm. The LTC of these structures were calculated using the HNEMD method in the temperature range of 200–500 K. To ensure the system remained within the linear response regime, the driving force parameter F_e was chosen as 5×10^{-5} Å^{-1}. A systematic analysis of different F_e values (see Supporting Information, Section 2) confirms that $F_e = 5 \times 10^{-5}$ Å^{-1} provides an optimal balance between numerical stability and adherence to linear-response conditions for Bi_2Te_3/Sb_2Te_3 SLs. All SL structures employed periodic boundary conditions in the x, y, and z directions, where 10 Å vacuum layers were added on both sides in the z direction to accurately simulate the thermal transport characteristics of finite-length SLs. Initially, the system was equilibrated in the NPT ensemble at 300 K and zero pressure for 1 ns to ensure the structure reached thermodynamic equilibrium. Subsequently, heat flow data were collected for 6 ns in the NVT ensemble using a Nosé–Hoover chain thermostat to maintain the target temperature, with a time step of 1 fs for statistical analysis. To ensure the reliability of our HNEMD results, we performed systematic convergence tests examining the effects of cross-sectional area, total system length, and simulation time on the calculated LTC (see Supporting Information, Section 2).

As shown in Fig. 5(a), the LTC of Bi_2Te_3/Sb_2Te_3 SLs exhibits pronounced non-monotonic behavior with period thickness, which is a

direct macroscopic manifestation of the phonon wave-particle duality transition. The LTC first decreases sharply with increasing period thickness, reaches a minimum value at a period thickness of approximately 5 nm, and then gradually increases. The MD-NEP predictions are consistent with other results [14,19,23]. Additionally, the high computational efficiency of the NEP model enables us to calculate SL systems with larger period thicknesses, revealing that when the period thickness exceeds 30 nm, the LTC continues to increase and gradually approaches that of bulk materials.

This non-monotonic behavior reveals the transition mechanism of phonon transport from incoherent (particlelike) to coherent (wavelike). In the long-period region (period thickness >5 nm), phonons exhibit particlelike behavior, where the interface spacing is much larger than the phonon coherence length. The system can be viewed as a series model of bulk thermal resistance and interfacial thermal resistance, with total thermal resistance equal to the sum of individual bulk thermal resistances and interfacial thermal resistances. When period thickness decreases (i.e., the number of interfaces per unit length increases), interfacial scattering increases, leading to a linear decrease in effective LTC, consistent with classical incoherent scattering theory predictions.

When the period thickness approaches the phonon coherence length, the wave nature of phonons begins to dominate, and the system enters the coherent transport regime. For acoustic phonons along the cross-plane direction, the group velocities are generally less than 2 km s^{-1} [Fig. 4(b)], yielding wavelengths of $\lambda = v_g/f \approx 1$–10 nm for the dominant heat-carrying phonons in the 0.2–2 THz frequency range. In this analysis, the phonon wavelength serves as an approximate proxy for the coherence length. The fact that these wavelengths are comparable to the critical period thickness (~5 nm) where the LTC minimum occurs provides evidence for the coherent transport picture. In this region, the periodic potential field leads to energy band folding effects in the phonon dispersion relation, forming miniband structures. As interface density further increases (period thickness decreases), the number of minibands decreases, but due to the redistribution of group velocities, the average phonon group velocity increases, leading to LTC recovery. However, to completely understand the microscopic mechanisms of phonon coherent effects in SLs, further analysis from the phonon mode level is needed to reveal the specific processes of interfacial reflection, transmission, and coherent interference. Therefore, subsequent sections will systematically analyze phonon transmission coefficients using phonon wave equations, elucidating phonon coherent scattering mechanisms at periodic heterogeneous interfaces from a wave dynamics perspective.

Temperature dependence analysis further reveals unique mechanisms of SL thermal transport. As shown in Fig. 5(b), by comparing LTC variations of SLs with different period thicknesses in the 200–500 K temperature range, we find that as temperature increases, the position where minimum LTC occurs in Bi_2Te_3/Sb_2Te_3 SLs remains essentially maintained near 5 nm. It is noteworthy that while the LTC of bulk Bi_2Te_3 and Sb_2Te_3 decreases as temperature increases from 200 K to 500 K (Fig. 3), Bi_2Te_3/Sb_2Te_3 SLs exhibit opposite behavior. This phenomenon primarily stems from the temperature-dependent enhancement of interfacial inelastic scattering processes. As temperature increases, phonon–phonon interactions and mode conversion processes at interfaces are enhanced, leading to significant increases in ITC [Fig. 4(d)], thereby causing overall LTC of SLs to increase with temperature. This contrasts sharply with the temperature dependence dominated by Umklapp scattering in bulk materials, highlighting the decisive role of interfacial effects in SL thermal transport.

Further analysis reveals that SLs with varying period thicknesses exhibit different temperature dependence behaviors. This difference is primarily attributed to the frequency-selective scattering effects dependent on period thickness: short-period SLs (<5 nm) mainly suppress low-frequency phonon transport through Bragg scattering conditions, and these phonons contribute relatively less at low temperatures but increase due to thermal excitation effects at high temperatures; long-period structures (>5 nm) mainly affect high-frequency short-wavelength phonons through interfacial roughness scattering, while high-frequency phonons respond relatively weakly to temperature changes. Due to fundamental differences in response mechanisms and contribution weights of different frequency phonons to temperature changes, this leads to the observed complex correlation between temperature dependence and period thickness.

This frequency-dependent scattering mechanism not only explains the temperature effect anomalies but also provides key clues for understanding SL phonon wave phenomena. Short-period SLs with observed coherent effects primarily stem from wave interference of low-frequency long-wavelength phonons, while long-period structures with incoherent scattering primarily affect high-frequency short-wavelength phonons. To thoroughly understand this complex frequency-period thickness-temperature three-dimensional correlation and its underlying microscopic physical mechanisms, detailed spectral LTC decomposition analysis is necessary, which will be systematically investigated in the next section through spectral LTC decomposition methods.

The coherent-to-incoherent phonon transport transition observed in Bi_2Te_3/Sb_2Te_3 SLs is expected to be a general phenomenon in other chalcogenide and thermoelectric heterostructures. Similar non-monotonic LTC behavior has been reported in several SLs [61]. The critical period thickness at which the LTC minimum occurs is primarily determined by the phonon mean free path (MFP) or coherence length of the dominant heat-carrying phonons. For Bi_2Te_3/Sb_2Te_3 SLs, this critical thickness remains around 5 nm across the temperature range of 200–500 K [Fig. 5(b)], suggesting that the coherent transport regime is relatively robust against temperature variations within this range.

However, factors such as carrier doping, which modifies electron–phonon interactions and reduces phonon MFPs, or interface roughness and intermixing, which enhance diffuse scattering and shorten the effective coherence length, could shift or broaden the transition region. The strength of coherence phenomena is governed by several key factors, including the acoustic impedance mismatch between constituent materials, the sharpness of interfaces, and the intrinsic phonon MFPs of the bulk materials. The relatively small acoustic contrast between Bi_2Te_3 and Sb_2Te_3, combined with their similar lattice structures, leads to moderate interfacial reflection and well-defined coherent interference effects. Systems with larger acoustic mismatch (e.g., Si/Ge) may exhibit stronger coherence effects but also more pronounced incoherent scattering at rough interfaces.

These considerations suggest that the coherence engineering strategy demonstrated here could be extended to other thermoelectric material systems, with the optimal SL design depending on the specific phonon properties and interface characteristics of the constituent materials.

3.4. Spectral lattice thermal conductivity decomposition

To provide microscopic-level interpretation of the minimum LTC phenomenon observed in Fig. 5 and elucidate the coherent-to-incoherent phonon transport transition mechanism in Bi_2Te_3/Sb_2Te_3 SLs, we calculated the spectral LTC of SLs with different period thicknesses in the temperature range of 200–500 K using the MD-NEP method, and compared it with the spectral LTC of pure Bi_2Te_3 and Sb_2Te_3. As shown in Fig. 6, the LTC of Bi_2Te_3 is primarily contributed by phonons in the 0–4 THz frequency range, while the phonon spectrum of Sb_2Te_3 extends over a broader range from 0–5 THz, which is highly consistent with the differences in their phonon DOS and group velocity distributions [Fig. 4(a) and (b)]. It is noteworthy that although the spectral LTC contribution of Sb_2Te_3 in the low-frequency region

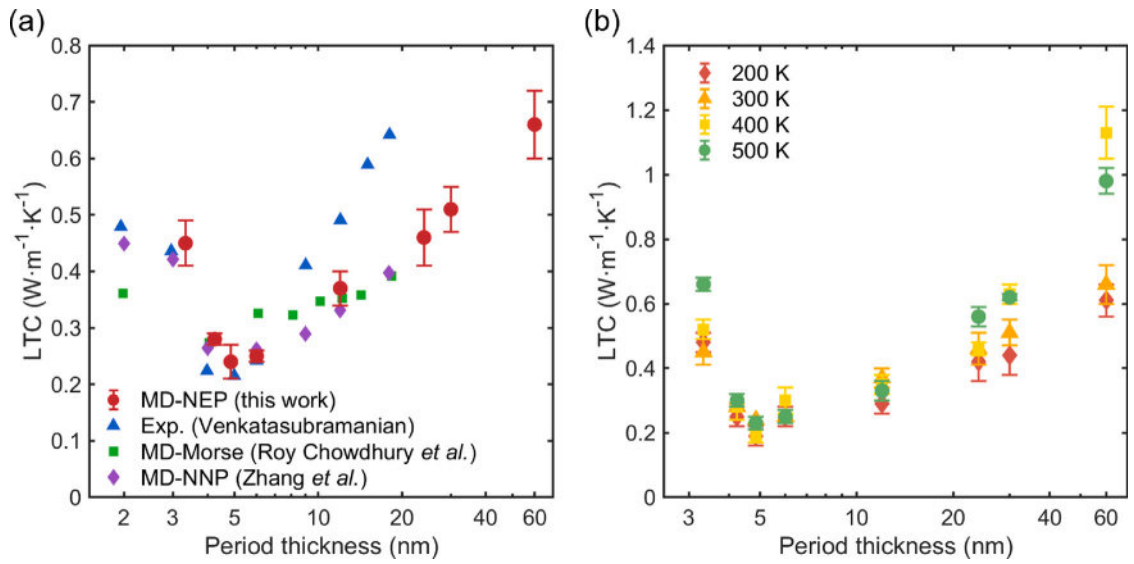

Fig. 5. (a) Variation of Bi_2Te_3/Sb_2Te_3 SL LTC with period thickness calculated using the MD-NEP method at 300 K, compared with experimental data and other numerical calculation results (MD-Morse potential and MD-NNP method) [14,19,23]. (b) Temperature-dependent variation of Bi_2Te_3/Sb_2Te_3 SL LTC with period thickness (200–500 K).

(0–2 THz) is slightly lower than that of Bi_2Te_3, mainly due to the relatively lighter mass of Sb atoms causing the phonon spectrum to shift toward higher frequencies and resulting in reduced low-frequency phonon density of states, Sb_2Te_3 exhibits significant LTC contributions in the high-frequency region (4–5 THz), making its overall LTC comparable to Bi_2Te_3. This difference in spectral distribution provides an important physical foundation for phonon mismatch and scattering at the interface. And the spectral LTC of both materials shows an overall decreasing trend with increasing temperature, but different frequency phonons exhibit distinct responses to temperature.

For Bi_2Te_3/Sb_2Te_3 SLs, spectral LTC analysis reveals the selective modulation effect of period thickness on phonon transport at different frequencies. As shown in Fig. 7, as period thickness increases from 3.33 nm to 60 nm, the spectral LTC of SLs first shows overall reduction followed by recovery, with variation trends completely consistent with those of total LTC. In the short-period region (3.33–4.85 nm), contributions from low-frequency phonons (0–2 THz) are significantly suppressed, which is directly related to the matching condition between phonon wavelength (or more accurately, coherence length) and SL period. When the SL period is comparable to the phonon wavelength, strong Bragg scattering occurs, leading to enhanced reflection of low-frequency long-wavelength phonons. Conversely, high-frequency phonons, due to their shorter wavelengths, are relatively less affected by periodic modulation. As period thickness further increases (≥6 nm), the system gradually transitions from coherent transport region to incoherent transport region, where the influence of interfacial scattering weakens and spectral LTC gradually recovers toward the average value of bulk materials. This frequency-dependent transport behavior provides direct microscopic evidence for understanding coherent effects in SLs. Temperature effects on SL spectral LTC exhibit complex frequency and period thickness dependencies. From 200 K to 500 K, different frequency phonons show significantly different response mechanisms. Contributions from low-frequency phonons overall show decreasing trends, mainly affected by enhanced anharmonic scattering; while high-frequency phonons in certain period thicknesses actually exhibit increasing trends, closely related to the temperature dependence of interfacial inelastic scattering processes.

To more clearly observe temperature effects, Fig. 8 presents the temperature-dependent variation of spectral LTC for SLs with different period thicknesses. However, analysis of the data in Fig. 8 reveals that phonon spectral LTC exhibits highly complex nonlinear characteristics in its response to temperature and period thickness, which cannot be explained by simple single mechanisms. SLs with varying period thicknesses demonstrate distinctly different behavior patterns in the temperature dependence of spectral LTC. Taking short-period structures (3.33–4.85 nm) as an example, low-frequency phonon (<2 THz) contributions show decreasing trends in the 200–400 K range but exhibit significant increases at 500 K. This non-monotonic behavior clearly indicates the presence of multiple competing scattering mechanisms. Under low-temperature conditions, coherent scattering effects may dominate, strongly suppressing low-frequency phonon transmission; while under high-temperature conditions, enhanced interfacial inelastic scattering processes and thermal excitation effects may fundamentally alter phonon transport characteristics, enabling low-frequency phonons to regain transmission capability. This difference reflects the extreme sensitivity of the matching condition between period thickness and phonon wavelength, where minor changes in geometric dimensions can lead to completely different Bragg scattering conditions and coherent interference effects. The effects of interfacial atomic mixing and aperiodic layer stacking on thermal transport are further examined in the Supporting Information (Sections 3 and 4) [69].

These complex interactions reflect the superposition effects of multiple physical mechanisms involved in phonon transport in SLs, including coherent Bragg scattering, incoherent interfacial scattering, phonon–phonon inelastic scattering, and temperature-activated interfacial transmission processes. Each mechanism has different weights and relative importance under various temperature and period thickness conditions, and their complex competition and synergy lead to the highly nonlinear behavior patterns observed, making simple phenomenological descriptions insufficient to cover all physical details. Analysis solely based on macroscopic spectral LTC is insufficient to completely resolve these microscopic mechanisms. A more intuitive and deeper physical picture may require combining phonon Green's functions or wave equation methods to further analyze from the phonon mode level, by calculating phonon energy transmission coefficients to reveal specific scattering behaviors of different frequencies, different incident angles, and different polarization mode phonons at periodic heterogeneous interfaces, thereby intuitively distinguishing the specific impacts of coherent interference, interfacial scattering, and mode conversion processes on spectral LTC distributions, and establishing a complete physical picture to explain the phonon wave-particle duality transition phenomena observed in SLs.

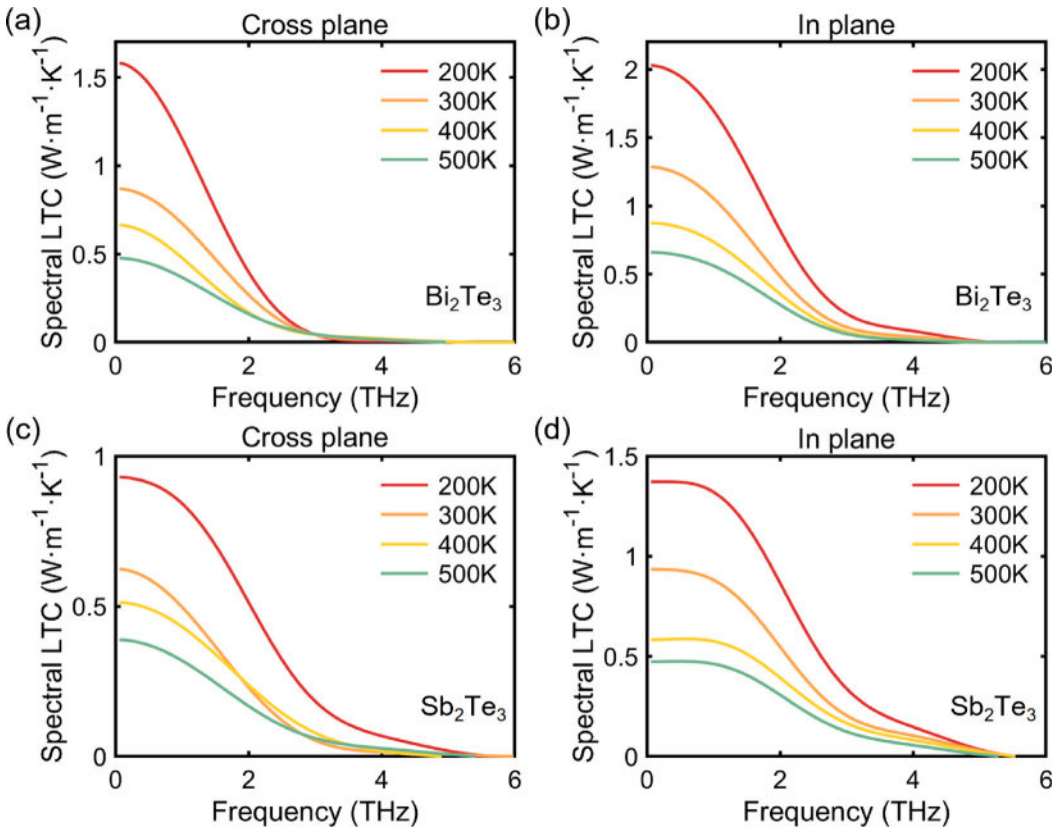

Fig. 6. Spectral LTC of Bi_2Te_3 and Sb_2Te_3 in cross-plane and in-plane directions at different temperatures calculated using MD-NEP simulations.

3.5. Wavelike (coherent) transport of phonons

The periodic interfacial arrays present in SL structures provide complex wave dynamics behavior for phonons. Wavelike (coherent) phonons undergo repeated reflection and refraction at multiple interfaces, generating interference effects similar to those in optics between different phonon waves, thereby significantly modulating the phonon transport process. To provide an intuitive explanation of this phenomenon, we employed the phonon wave equation and transfer matrix method described in Section 2.4, starting from elastic wave theory to systematically calculate the transmission characteristics of phonons in Bi_2Te_3/Sb_2Te_3 SLs.

We consider acoustic phonon modes propagating along the SL growth direction, namely the [001] crystallographic direction (Γ-Z direction). In this direction, the phonon dispersion relation contains one longitudinal mode and two degenerate transverse modes. Based on phonon dispersion relations obtained from DFT calculations, the longitudinal mode frequency range of Bi_2Te_3 spans from 0 to 6.08 THz, and the transverse mode frequency range spans from 0 to 4.09 THz; while for Sb_2Te_3, the longitudinal mode frequency range extends from 0 to 7.38 THz, and the transverse mode frequency range from 0 to 4.81 THz. The significantly lighter mass of Sb atoms compared to Bi atoms leads to the overall extension of the Sb_2Te_3 phonon spectrum toward higher frequency regions. When phonon waves of different frequency ranges undergo elastic scattering at interfaces, the acoustic impedance mismatch and spectral mismatch on both sides of the interface generate critical angles and cutoff frequencies, thereby significantly affecting phonon transmission and reflection behavior.

Fig. 9 presents the distribution of transmission coefficients for three phonon polarization modes (P wave, SV wave, SH wave) at a single Bi_2Te_3/Sb_2Te_3 interface as functions of frequency and incident angle. The color scale for transmission coefficients ranges from 0 (complete reflection) to 1 (complete transmission). SH waves exhibit relatively simple transmission characteristics. Since the displacement of SH waves is perpendicular to the incident plane, mode conversion does not occur, and their transmission behavior is primarily determined by the shear impedance mismatch between the two materials. Under conditions of low frequency and small incident angles, SH wave transmission coefficients are high (approaching 1), indicating that phonons can pass through the interface relatively easily. However, as the incident angle increases, particularly when exceeding a critical angle, the transmission coefficient drops sharply and approaches zero, resulting in total internal reflection. The situation for P and SV waves is relatively complex because these two modes undergo mutual conversion at the interface. Incident P waves can generate reflected P and SV waves, as well as transmitted P and SV waves, and vice versa. This mode conversion leads to energy redistribution among different polarization states. As observed in Fig. 9, P and SV waves exhibit complex frequency-angle dependent transmission coefficients, with resonant phenomena of transmission enhancement occurring under certain specific conditions, attributed to the stress continuity conditions at the interface and phase matching of different mode waves.

Total internal reflection effects are significantly present in all three modes. Due to the group velocity mismatch between Bi_2Te_3 and Sb_2Te_3 [Fig. 4(b)], when phonons are incident from low-velocity medium A to high-velocity medium B, a critical angle $\theta_c = \arcsin\left(\frac{v_A}{v_B}\right)$ is generated [70,71]. When the incident angle exceeds the critical angle, total internal reflection occurs and the transmission coefficient becomes zero. It should be noted that the phase velocity $v_p(\omega) = \frac{\omega}{k}$ is frequency-dependent, and the critical angle also varies with frequency. The results in regions of zero transmission coefficient at large incident angles and high frequencies, indicating that phonon waves under these conditions are completely reflected, converted to surface waves propagating along the interface and gradually decay, contributing nothing to heat transport in the direction perpendicular to the interface.

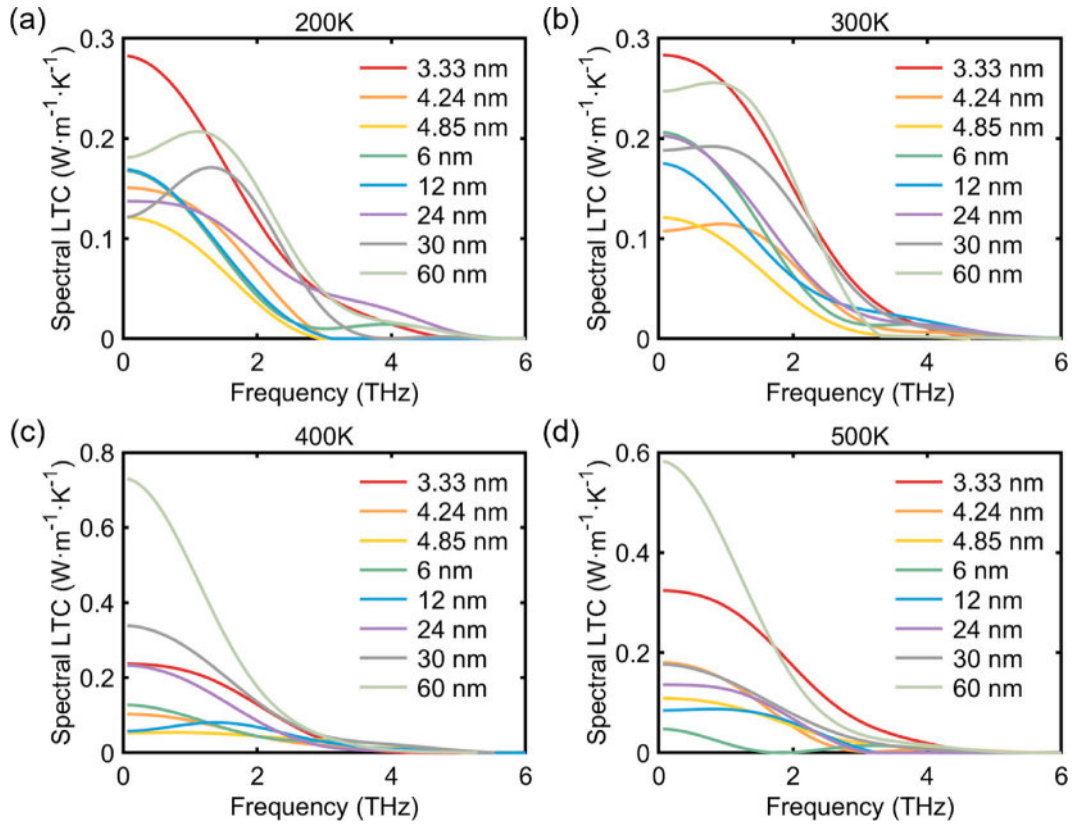

Fig. 7. Variation of spectral LTC of Bi_2Te_3/Sb_2Te_3 SLs with period thickness at 200–500 K.

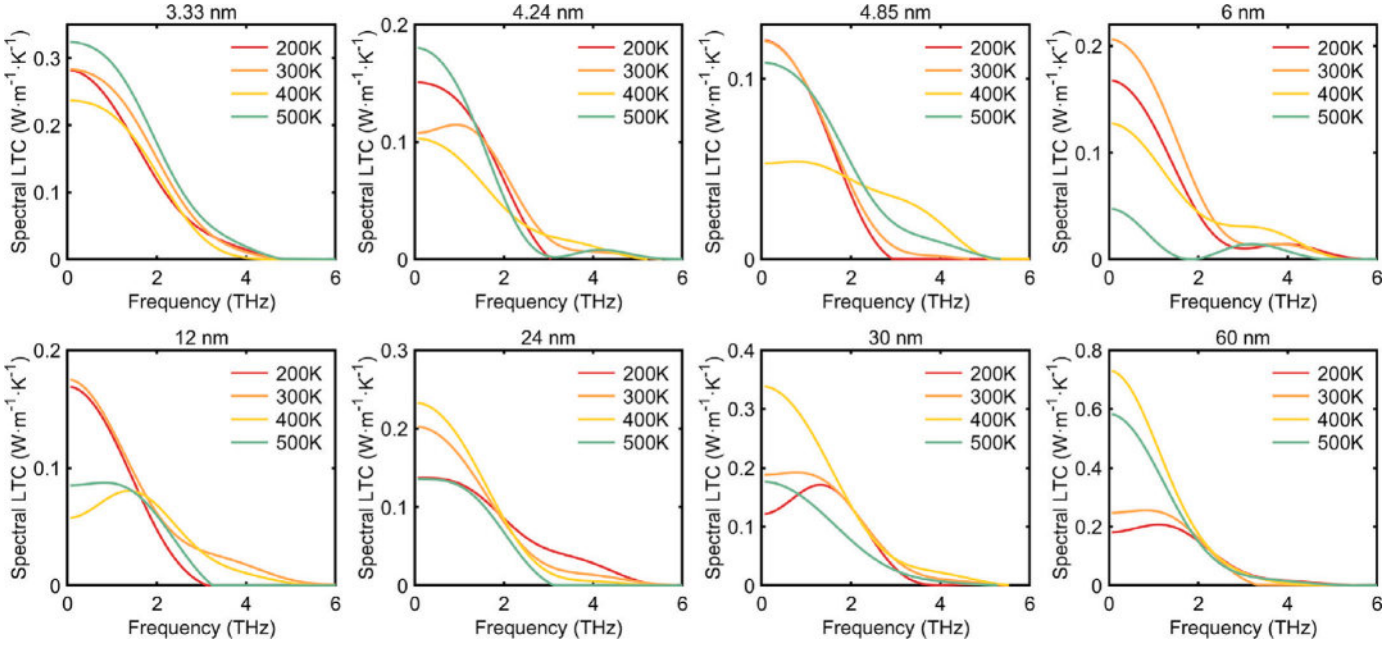

Fig. 8. Evolution of spectral LTC with temperature for Bi_2Te_3/Sb_2Te_3 SLs of different period thicknesses. This plot shows from another perspective the complex correlations between temperature, period thickness, and phonon frequency, revealing the multi-dimensional control mechanisms of phonon transport in SLs.

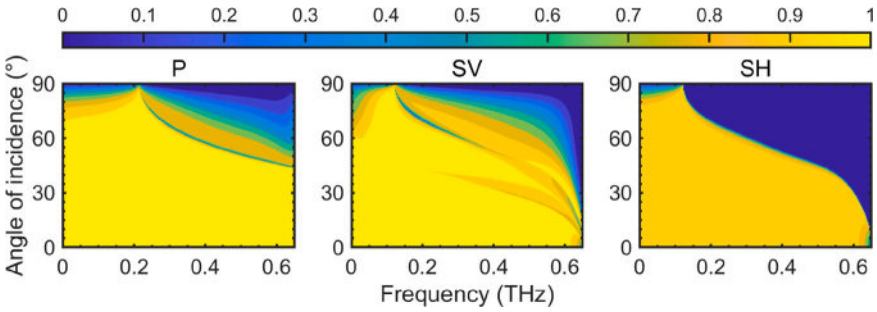

Fig. 9. Phonon transmission coefficients at a single Bi_2Te_3/Sb_2Te_3 interface. Transmission coefficient values are represented by color scale (range from 0 to 1), depending on phonon polarization, frequency, and angle of incidence. From left to right: P wave, SV wave, and SH wave. (For interpretation of the references to color in this figure legend, the reader is referred to the web version of this article.)

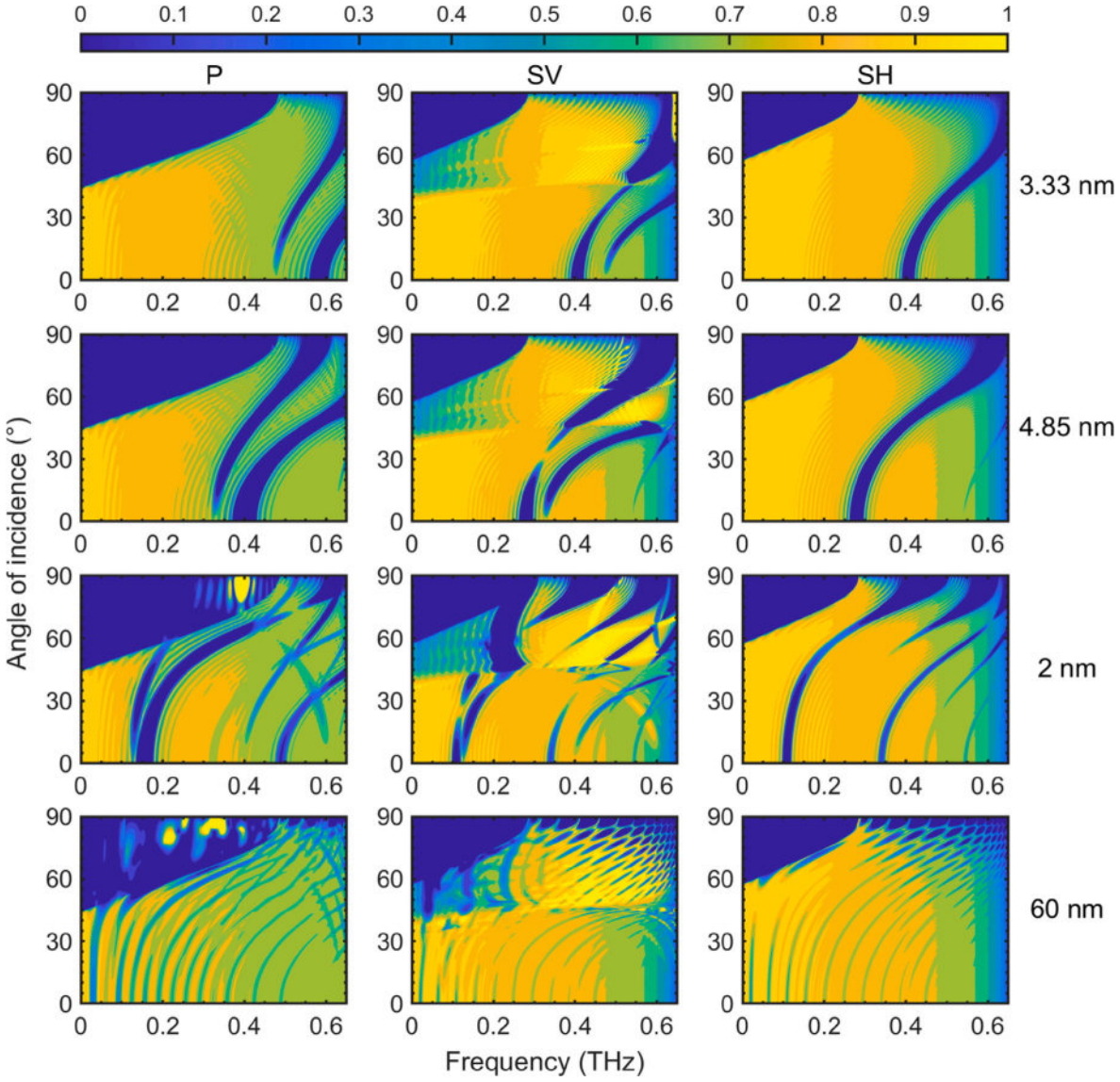

Fig. 10. Evolution of phonon transmission coefficients in Bi_2Te_3/Sb_2Te_3 SLs with period thickness (3.33–60 nm) for a fixed total length of 120 nm (corresponding to the model in Section 3.C).

Fig. 10 shows the evolution of phonon transmission coefficients with period thickness (3.33–60 nm) in Bi_2Te_3/Sb_2Te_3 SLs with a fixed total length of 120 nm. This result directly corresponds to the non-monotonic LTC variation behavior observed in Fig. 5, revealing the underlying microscopic physical mechanisms from a wave dynamics perspective. It should be noted that transmission coefficient calculations based on phonon wave equations only reflect the wavelike transport characteristics of coherent phonons and do not include contributions from incoherent particle scattering processes.

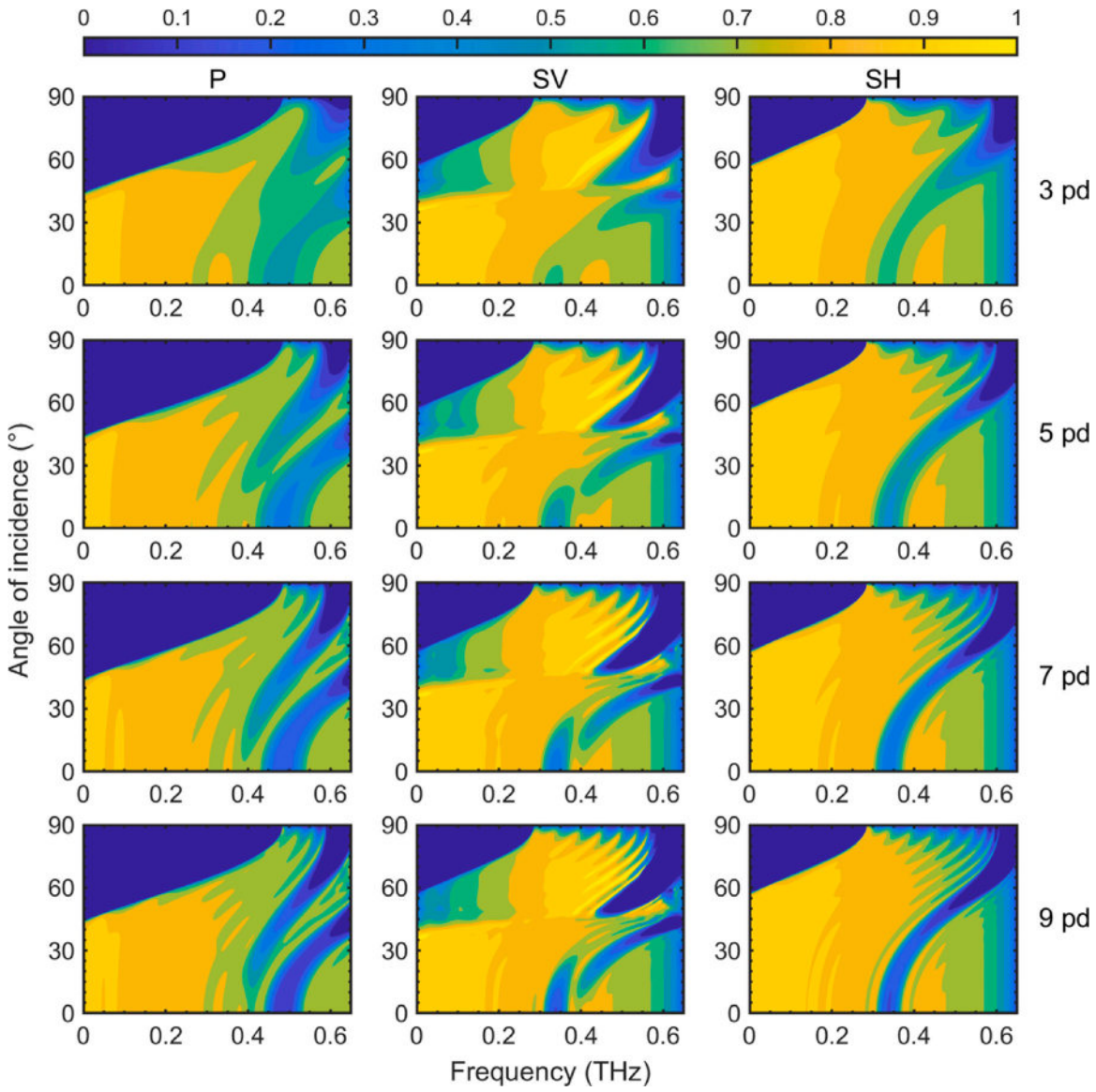

Fig. 11. Evolution of Bi_2Te_3/Sb_2Te_3 SLs with a fixed period thickness of 4 nm for different numbers of periods (3, 5, 7, 9 periods).

When the period thickness approaches or is smaller than the wavelength of the primary heat-carrying phonons (approximately 2–5 nm), coherent effects dominate. At this point, phonon waves undergo multiple reflections between adjacent interfaces, forming clear interference fringe patterns. Frequency-angle combinations satisfying Bragg scattering conditions $2d \sin\theta = n\lambda$ (where d is the period thickness, n is an integer, and λ is the wavelength) result in destructive interference leading to transmission minima, forming phonon bandgaps or forbidden band structures. These bandgaps are analogous to electronic band structures in periodic potentials, strongly suppressing phonon transmission at specific frequencies. Due to the period thickness dependence of Bragg conditions, SLs with different periods exhibit significantly different bandgap distribution characteristics, including the position, number, width, and shape of bandgaps.

In the short-period range, as period thickness increases from 3.33 nm to 4.85 nm, bandgap positions can be observed to shift overall toward lower frequency directions, meaning coherent scattering begins to block longer wavelength phonon modes. Simultaneously, bandgap widths significantly broaden, forming suppressive effects over wider frequency ranges. This change has important thermal transport implications. Combined with spectral LTC decomposition results in Figs. 6–8, low-frequency phonons (0–2 THz) contribute significantly to the LTC of Bi_2Te_3/Sb_2Te_3 SLs. Therefore, when bandgaps shift toward low frequencies and broaden, the blocking effect of coherent interference on primary heat-carrying phonons gradually increases, leading to continuous reduction in coherent phonon contributions to total LTC. This trend reveals how increasing period thickness enhances suppressive effects on heat transport through optimizing Bragg scattering conditions in the coherent-dominated short-period regime.

As period thickness continues to increase from 4.85 nm to 60 nm, with the total length fixed at 120 nm, the number of SL periods decreases accordingly from approximately 25 to 2. This leads to systematic changes in the bandgap structure: the number of bandgaps decreases significantly, interference fringes become sparse, and the frequency width of individual bandgaps narrows. These changes indicate that the overall suppressive effect of the SL structure on wavelike phonons gradually weakens. More importantly, when the period thickness exceeds the phonon coherence length (approximately 5 nm), phase

correlations between adjacent interfaces begin to be lost. Although transmission coefficient patterns based on wave equations still exhibit wavelike characteristics, the actual heat transport process has gradually transitioned toward mechanisms dominated by incoherent particle scattering. In this regime, the weakening of coherent interference effects and the cumulative effects of incoherent interfacial scattering jointly determine the slow recovery trend of LTC.

To further elucidate the effect of increasing interface numbers on coherent interference, Fig. 11 shows the evolution of phonon transmission coefficients with the number of periods (3, 5, 7, 9 periods) when the period thickness is fixed at 4 nm (close to the minimum LTC position where the system is in the coherent-dominated regime). As the number of periods increases from 3 to 9, transmission coefficient distributions exhibit significant systematic reduction. Additionally, the clarity and sharpness of interference fringes improve significantly with increasing period numbers. More interfaces cause more reflected waves to undergo coherent superposition, leading to greatly enhanced contrast between transmission peaks formed by constructive interference and transmission valleys formed by destructive interference. In the 9-period structure, bandgap regions become narrower but deeper compared to the 3-period structure, indicating that phonon frequency selectivity is significantly enhanced. Specific frequency phonons are nearly completely blocked, while phonons at adjacent allowed frequencies can pass through relatively freely, forming sharp transmission boundaries. The results in Fig. 11 clearly demonstrate that in the period thickness range dominated by coherence, increasing the number of interfaces can effectively enhance interference effects, making phonon forbidden bands more distinct and frequency selectivity stronger, with overall transmission coefficients lower. Through precise control of SL period numbers and period thickness, targeted modulation of specific frequency phonons can be achieved.

The MD-NEP method, based on interatomic potentials containing harmonic and anharmonic terms, naturally captures comprehensive effects of various mechanisms including phonon interfacial scattering, wavelike transport, and phonon–phonon inelastic scattering, enabling accurate prediction of LTC and temperature dependence for SLs with different period thicknesses. Wave-based approaches such as phonon wave equations or Green's function methods can clearly demonstrate, at the frequency-angle-polarization mode level, the formation of bandgap structures by coherent phonons in periodic interfacial arrays and the systematic evolution of these bandgaps with geometric parameters, providing complementary microscopic physical insights to understand the minimum LTC phenomenon observed in MD simulations. [46,72,73].

4. Summary and conclusions

This study employed NEP combined with large-scale MD simulations to systematically investigate the thermal transport properties of Bi_2Te_3/Sb_2Te_3 SLs. The constructed NEP model demonstrates sufficient accuracy and reliability for predicting the thermal transport properties of both bulk Bi_2Te_3, Sb_2Te_3 and their heterostructures, with predicted LTC showing good agreement with experimental and theoretical data in the temperature range of 200–500 K. The investigation reveals that Bi_2Te_3/Sb_2Te_3 SLs exhibit a minimum LTC at a period thickness of approximately 5 nm, with LTC displaying pronounced non-monotonic variation with period thickness. This phenomenon represents a fundamental characteristic of the transition from coherent wavelike phonon transport to incoherent particlelike scattering. Spectral decomposition of LTC provides key insights into the frequency-dependent characteristics of phonon transport modulation in SLs. Low-frequency phonons are primarily influenced by coherent interference effects and exhibit strong period thickness dependence, while high-frequency phonons are mainly modulated through incoherent interfacial scattering processes. Temperature effects on phonons of different frequencies exhibit fundamental differences in their response mechanisms, with low-frequency phonons showing relatively weak temperature dependence while high-frequency phonons demonstrate stronger temperature sensitivity, a phenomenon related to the distinct scattering mechanisms in different frequency regimes. Phonon wave equation calculations elucidate the wavelike phonon transport phenomena in SLs from a wave dynamics perspective. Transmission coefficient analysis reveals that Bragg scattering conditions form phonon bandgaps at specific frequency-angle combinations, leading to selective phonon blocking. With systematic variation of period thickness, the position, number, and width of bandgaps exhibit clear evolutionary patterns, providing direct interpretation of how coherent interference modulates thermal transport. Increasing the number of interfaces can effectively enhance interference effects, making phonon forbidden bands more distinct, frequency selectivity stronger, and overall transmission coefficients lower.

The MD-NEP method, based on interatomic potentials containing harmonic and anharmonic terms, naturally captures the comprehensive effects of various mechanisms including phonon interfacial scattering, wavelike transport, and phonon–phonon inelastic scattering, enabling accurate prediction of LTC and temperature dependence for SLs with different period thicknesses. Phonon wave equation analysis can clearly demonstrate at the frequency-angle-polarization mode level how coherent phonons form bandgap structures in periodic interfacial arrays and how these bandgaps systematically evolve with geometric parameters, providing complementary microscopic physical insights to understand the minimum LTC phenomenon observed in MD simulations. The research results also provide a theoretical foundation for interface engineering and performance optimization of broader nanostructured thermoelectric materials. Through precise control of SL period thickness and interface density, targeted modulation of specific frequency phonons can be achieved, offering beneficial insights for developing high-performance thermoelectric devices with ultra-low thermal conductivity.

CRediT authorship contribution statement

Bin Liu: Writing – original draft, Validation, Investigation. **Zhiguo Tian:** Validation, Software. **Alexander A. Barinov:** Writing – review & editing, Software, Resources. **Moran Wang:** Writing – review & editing, Supervision, Funding acquisition, Conceptualization.

Declaration of competing interest

The authors declare that they have no known competing financial interests or personal relationships that could have appeared to influence the work reported in this paper.

Acknowledgments

This work is supported by the Beijing Natural Science Foundation, China (Grant No. 3254051), the China Postdoctoral Science Foundation (Grant No. 2023M741895) and the Tsinghua University Initiative Scientific Research Program, China. The numerical calculations in this paper have been done on the "Explorer 1000" high-performance computing cluster at the High-Performance Computing Center of Tsinghua University, China.

Appendix A. Supplementary data

Supplementary material related to this article can be found online at https://doi.org/10.1016/j.ijheatmasstransfer.2025.128283.

Data availability

The training dataset will be made freely available at https://github.com/binliu93/Data_for_Bi2Te3-Sb2Te3.

References

[1] X. Shi, J. Zou, Z. Chen, Advanced thermoelectric design: From materials and structures to devices, Chem. Rev. 120 (15) (2020) 7399–7515, http://dx.doi.org/10.1021/acs.chemrev.0c00026.

[2] J. Feng, J. Li, R. Liu, Low-temperature thermoelectric materials and applications, Nano Energy 126 (2024) 109651, http://dx.doi.org/10.1016/j.nanoen.2024.109651.

[3] X. Wan, W. Feng, Y. Wang, H. Wang, X. Zhang, C. Deng, N. Yang, Materials discovery and properties prediction in thermal transport via materials informatics: A mini review, Nano Lett. 19 (6) (2019) 3387–3395, http://dx.doi.org/10.1021/acs.nanolett.8b05196.

[4] X. Wan, D. Pan, Z. Zong, Y. Qin, J.-T. Lü, S. Volz, L. Zhang, N. Yang, Modulating thermal conductivity via targeted phonon excitation, Nano Lett. 24 (23) (2024) 6889–6896, http://dx.doi.org/10.1021/acs.nanolett.4c00478.

[5] V.D. Blank, S.G. Buga, V.A. Kulbachinskii, V.G. Kytin, V.V. Medvedev, M.Y. Popov, P.B. Stepanov, V.F. Skok, Thermoelectric properties of Bi0.5Sb1.5Te3/C60 nanocomposites, Phys. Rev. B 86 (7) (2012) 075426, http://dx.doi.org/10.1103/PhysRevB.86.075426.

[6] N.A. Katcho, N. Mingo, D.A. Broido, Lattice thermal conductivity of (Bi1-xSbx)2Te3 alloys with embedded nanoparticles, Phys. Rev. B 85 (11) (2012) 115208, http://dx.doi.org/10.1103/PhysRevB.85.115208.

[7] Y. Liu, Y. Zhang, S. Ortega, M. Ibáñez, K.H. Lim, A. Grau-Carbonell, S. Martí-Sánchez, K.M. Ng, J. Arbiol, M.V. Kovalenko, D. Cadavid, A. Cabot, Crystallographically textured nanomaterials produced from the liquid phase sintering of BixSb2–xTe3 nanocrystal building blocks, Nano Lett. 18 (4) (2018) 2557–2563, http://dx.doi.org/10.1021/acs.nanolett.8b00263.

[8] J. Ballard, M. Hubbard, S.-J. Jung, V. Rojas, R. Ung, J. Suh, M. Kim, J. Lee, J.M. Pierce, R. Venkatasubramanian, Nano-engineered thin-film thermoelectric materials enable practical solid-state refrigeration, Nat. Commun. 16 (1) (2025) 4421, http://dx.doi.org/10.1038/s41467-025-59698-y.

[9] J. Fu, J. Huang, F. Bernard, Electronic structure, elastic and optical properties of Bi2Te3/Sb2Te3 thermoelectric composites in the periodic-superlattice thin films, Compos. Commun. 28 (2021) 100917, http://dx.doi.org/10.1016/j.coco.2021.100917.

[10] N. Goyal, K. Jagadish, N. Ravishankar, Defect-mediated growth of layered lateral Bi2Te3–Sb2Te3–Bi2Te3 heterostructures, J. Phys. Chem. C 128 (18) (2024) 7784–7794, http://dx.doi.org/10.1021/acs.jpcc.4c01472.

[11] Z. Ju, C. Crawford, J. Adamczyk, E.S. Toberer, S.M. Kauzlarich, Study of the thermoelectric properties of Bi2Te3/Sb2Te3 core–shell heterojunction nanostructures, ACS Appl. Mater. Interfaces 14 (21) (2022) 24886–24896, http://dx.doi.org/10.1021/acsami.2c03011.

[12] T.Q. Kimberly, K.M. Ciesielski, X. Qi, E.S. Toberer, S.M. Kauzlarich, High thermoelectric performance in 2D Sb2Te3 and Bi2Te3 nanoplate composites enabled by energy carrier filtering and low thermal conductivity, ACS Appl. Electron. Mater. 6 (5) (2024) 2816–2825, http://dx.doi.org/10.1021/acsaelm.3c00385.

[13] M.N. Touzelbaev, P. Zhou, R. Venkatasubramanian, K.E. Goodson, Thermal characterization of Bi2Te3/Sb2Te3 superlattices, J. Appl. Phys. 90 (2) (2001) 763–767, http://dx.doi.org/10.1063/1.1374458.

[14] R. Venkatasubramanian, Lattice thermal conductivity reduction and phonon localizationlike behavior in superlattice structures, Phys. Rev. B 61 (4) (2000) 3091–3097, http://dx.doi.org/10.1103/PhysRevB.61.3091.

[15] R. Venkatasubramanian, E. Siivola, T. Colpitts, B. O'Quinn, Thin-film thermoelectric devices with high room-temperature figures of merit, Nature 413 (6856) (2001) 597–602, http://dx.doi.org/10.1038/35098012.

[16] Z. Zhang, Y. Guo, M. Bescond, M. Nomura, S. Volz, J. Chen, Assessing phonon coherence using spectroscopy, Phys. Rev. B 107 (15) (2023) 155426, http://dx.doi.org/10.1103/PhysRevB.107.155426.

[17] Z. Zhang, Y. Guo, M. Bescond, J. Chen, M. Nomura, S. Volz, How coherence is governing diffuson heat transfer in amorphous solids, npj Comput. Mater. 8 (1) (2022) 96, http://dx.doi.org/10.1038/s41524-022-00776-w.

[18] Z. Zhang, Y. Guo, M. Bescond, J. Chen, M. Nomura, S. Volz, Generalized decay law for particlelike and wavelike thermal phonons, Phys. Rev. B 103 (18) (2021) 184307, http://dx.doi.org/10.1103/PhysRevB.103.184307.

[19] P. Roy Chowdhury, J. Shi, T. Feng, X. Ruan, Prediction of Bi2Te3-Sb2Te3 interfacial conductance and superlattice thermal conductivity using molecular dynamics simulations, ACS Appl. Mater. Interfaces 13 (3) (2021) 4636–4642, http://dx.doi.org/10.1021/acsami.0c17851.

[20] Y. Ouyang, C. Yu, J. He, P. Jiang, W. Ren, J. Chen, Accurate description of high-order phonon anharmonicity and lattice thermal conductivity from molecular dynamics simulations with machine learning potential, Phys. Rev. B 105 (11) (2022) 115202, http://dx.doi.org/10.1103/PhysRevB.105.115202.

[21] H. Xie, X. Gu, H. Bao, Effect of the accuracy of interatomic force constants on the prediction of lattice thermal conductivity, Comput. Mater. Sci. 138 (2017) 368–376, http://dx.doi.org/10.1016/j.commatsci.2017.06.047.

[22] P. Zhang, F. Lyu, D. Jin, Z. Zhang, S. Chen, Y. Liu, Z. Wang, Z. Lu, S. Liang, R. Xiong, Phonon thermal transport in Bi2Te3/Sb2Te3 monolayer superlattices: a neural network potential study, Nanoscale 17 (5) (2025) 2718–2727, http://dx.doi.org/10.1039/D4NR04968C.

[23] P. Zhang, M. Qin, Z. Zhang, D. Jin, Y. Liu, Z. Wang, Z. Lu, J. Shi, R. Xiong, Accessing the thermal conductivities of Sb2Te3 and Bi2Te3/Sb2Te3 superlattices by molecular dynamics simulations with a deep neural network potential, Phys. Chem. Chem. Phys. 25 (8) (2023) 6164–6174, http://dx.doi.org/10.1039/D2CP05590B.

[24] Z. Fan, Z. Zeng, C. Zhang, Y. Wang, K. Song, H. Dong, Y. Chen, T. Ala-Nissila, Neuroevolution machine learning potentials: Combining high accuracy and low cost in atomistic simulations and application to heat transport, Phys. Rev. B 104 (10) (2021) 104309, http://dx.doi.org/10.1103/PhysRevB.104.104309.

[25] P. Ying, W. Zhou, L. Svensson, E. Berger, E. Fransson, F. Eriksson, K. Xu, T. Liang, J. Xu, B. Song, S. Chen, P. Erhart, Z. Fan, Highly efficient path-integral molecular dynamics simulations with GPUMD using neuroevolution potentials: Case studies on thermal properties of materials, J. Chem. Phys. 162 (6) (2025) 064109, http://dx.doi.org/10.1063/5.0241006.

[26] X. Zhou, Y. Liu, B. Tang, J. Wang, H. Dong, X. Xiu, S. Chen, Z. Fan, Million-atom heat transport simulations of polycrystalline graphene approaching first-principles accuracy enabled by neuroevolution potential on desktop GPUs, J. Appl. Phys. 137 (1) (2025) 014305, http://dx.doi.org/10.1063/5.0244987.

[27] P.E. Blöchl, Projector augmented-wave method, Phys. Rev. B 50 (24) (1994) 17953–17979, http://dx.doi.org/10.1103/PhysRevB.50.17953.

[28] J.P. Perdew, K. Burke, M. Ernzerhof, Generalized gradient approximation made simple, Phys. Rev. Lett. 77 (18) (1996) 3865–3868, http://dx.doi.org/10.1103/PhysRevLett.77.3865.

[29] S. Grimme, J. Antony, S. Ehrlich, H. Krieg, A consistent and accurate ab initio parametrization of density functional dispersion correction (DFT-D) for the 94 elements H-Pu, J. Chem. Phys. 132 (15) (2010) 154104, http://dx.doi.org/10.1063/1.3382344.

[30] P. Zhang, Z. Zhang, Y. Liu, Z. Wang, Z. Lu, R. Xiong, Phonon thermal transport in Bi2Te3 from a deep-neural-network interatomic potential, Phys. Rev. Appl. 18 (5) (2022) 054022, http://dx.doi.org/10.1103/PhysRevApplied.18.054022.

[31] P. Zhang, W. Liao, Z. Zhu, M. Qin, Z. Zhang, D. Jin, Y. Liu, Z. Wang, Z. Lu, R. Xiong, Tuning the lattice thermal conductivity of Sb2Te3 by Cr doping: a deep potential molecular dynamics study, Phys. Chem. Chem. Phys. 25 (22) (2023) 15422–15432, http://dx.doi.org/10.1039/D3CP00999H.

[32] A. Togo, First-principles phonon calculations with phonopy and phono3py, J. Phys. Soc. Japan 92 (1) (2023) 012001, http://dx.doi.org/10.7566/JPSJ.92.012001.

[33] A. Togo, L. Chaput, T. Tadano, I. Tanaka, Implementation strategies in phonopy and phono3py, J. Phys.: Condens. Matter. 35 (35) (2023) 353001, http://dx.doi.org/10.1088/1361-648X/acd831.

[34] T. Liang, K. Xu, E. Lindgren, Z. Chen, R. Zhao, J. Liu, B. Tang, B. Zhang, Y. Wang, K. Song, P. Ying, H. Dong, S. Chen, P. Erhart, Z. Fan, T. Ala-Nissila, J. Xu, NEP89: Universal neuroevolution potential for inorganic and organic materials across 89 elements, 2025, http://dx.doi.org/10.48550/arXiv.2504.21286, arXiv preprint.

[35] K. Xu, H. Bu, S. Pan, E. Lindgren, Y. Wu, Y. Wang, J. Liu, K. Song, B. Xu, Y. Li, T. Hainer, L. Svensson, J. Wiktor, R. Zhao, H. Huang, C. Qian, S. Zhang, Z. Zeng, B. Zhang, B. Tang, Y. Xiao, Z. Yan, J. Shi, Z. Liang, J. Wang, T. Liang, S. Cao, Y. Wang, P. Ying, N. Xu, C. Chen, Y. Zhang, Z. Chen, X. Wu, W. Jiang, E. Berger, Y. Li, S. Chen, A.J. Gabourie, H. Dong, S. Xiong, N. Wei, Y. Chen, J. Xu, F. Ding, Z. Sun, T. Ala-Nissila, A. Harju, J. Zheng, P. Guan, P. Erhart, J. Sun, W. Ouyang, Y. Su, Z. Fan, GPUMD 4.0: A high-performance molecular dynamics package for versatile materials simulations with machine-learned potentials, Mater. Genome Eng. Adv. (2025) e70028, http://dx.doi.org/10.1002/mgea.70028.

[36] C. Chen, Y. Li, R. Zhao, Z. Liu, Z. Fan, G. Tang, Z. Wang, NepTrain and NepTrainKit: Automated active learning and visualization toolkit for neuroevolution potentials, Comput. Phys. Comm. 317 (2025) 109859, http://dx.doi.org/10.1016/j.cpc.2025.109859.

[37] J. Tian, Y. Li, P. Zhang, F. Lyu, S. Chen, Y. Liu, Z. Wang, Z. Lu, S. Liang, R. Xiong, Unexpected enhanced thermal conductivity of 1–1 Sb2Te3/Cr2Te3 monolayer superlattice: a comparative study with Sb2Te3 monolayer, Chem. Phys. Lett. 879 (2025) 142382, http://dx.doi.org/10.1016/j.cplett.2025.142382.

[38] Z. Fan, H. Dong, A. Harju, T. Ala-Nissila, Homogeneous nonequilibrium molecular dynamics method for heat transport and spectral decomposition with many-body potentials, Phys. Rev. B 99 (6) (2019) 064308, http://dx.doi.org/10.1103/PhysRevB.99.064308.

[39] A.J. Gabourie, Z. Fan, T. Ala-Nissila, E. Pop, Spectral decomposition of thermal conductivity: Comparing velocity decomposition methods in homogeneous molecular dynamics simulations, Phys. Rev. B 103 (20) (2021) 205421, http://dx.doi.org/10.1103/PhysRevB.103.205421.

[40] H. Bao, J. Chen, X. Gu, B. Cao, A review of simulation methods in micro/nanoscale heat conduction, ES Energy Environ. 1 (2018) 16–55, http://dx.doi.org/10.30919/esee8c149.

[41] S. Hu, M. An, N. Yang, B. Li, Manipulating the temperature dependence of the thermal conductivity of graphene phononic crystal, Nanotechnology 27 (26) (2016) 265702, http://dx.doi.org/10.1088/0957-4484/27/26/265702.

[42] D. Ma, X. Wan, N. Yang, Unexpected thermal conductivity enhancement in pillared graphene nanoribbon with isotopic resonance, Phys. Rev. B 98 (24) (2018) 245420, http://dx.doi.org/10.1103/PhysRevB.98.245420.

[43] P. Roy Chowdhury, X. Ruan, Unexpected thermal conductivity enhancement in aperiodic superlattices discovered using active machine learning, npj Comput. Mater. 8 (1) (2022) 12, http://dx.doi.org/10.1038/s41524-022-00701-1.
[44] H. Wei, Y. Hu, H. Bao, X. Ruan, Quantifying the diverse wave effects in thermal transport of nanoporous graphene, Carbon 197 (2022) 18–26, http://dx.doi.org/10.1016/j.carbon.2022.06.011.
[45] L. Yang, N. Yang, B. Li, Extreme low thermal conductivity in nanoscale 3D Si phononic crystal with spherical pores, Nano Lett. 14 (4) (2014) 1734–1738, http://dx.doi.org/10.1021/nl403750s.
[46] Y. Guo, M. Bescond, Z. Zhang, S. Xiong, K. Hirakawa, M. Nomura, S. Volz, Thermal conductivity minimum of graded superlattices due to phonon localization, APL Mater. 9 (9) (2021) 091104, http://dx.doi.org/10.1063/5.0054921.
[47] B. Liu, Y. Guo, V.I. Khvesyuk, A.A. Barinov, M. Wang, Heat conduction of multilayer nanostructures with consideration of coherent and incoherent phonon transport, Nano Res. 15 (10) (2022) 9492–9497, http://dx.doi.org/10.1007/s12274-022-4589-7.
[48] Z. Zhang, Y. Guo, M. Bescond, J. Chen, M. Nomura, S. Volz, Heat conduction theory including phonon coherence, Phys. Rev. Lett. 128 (1) (2022) 015901, http://dx.doi.org/10.1103/PhysRevLett.128.015901.
[49] Y. Guo, M. Bescond, Z. Zhang, M. Luisier, M. Nomura, S. Volz, Quantum mechanical modeling of anharmonic phonon-phonon scattering in nanostructures, Phys. Rev. B 102 (19) (2020) 195412, http://dx.doi.org/10.1103/PhysRevB.102.195412.
[50] P. Pereyra, The transfer matrix method and the theory of finite periodic systems. from heterostructures to superlattices, Phys. Status Solidi (b) 259 (3) (2022) 2100405, http://dx.doi.org/10.1002/pssb.202100405.
[51] S. Tamura, D.C. Hurley, J.P. Wolfe, Acoustic-phonon propagation in superlattices, Phys. Rev. B 38 (2) (1988) 1427–1449, http://dx.doi.org/10.1103/PhysRevB.38.1427.
[52] G. Chen, Nanoscale Energy Transport and Conversion: A Parallel Treatment of Electrons, Molecules, Phonons, and Photons, Oxford University Press, 2005.
[53] J. Achenbach, Wave Propagation in Elastic Solids, North-Holland Publishing Company, Amsterdam, 1973.
[54] B. Auld, Acoustic Fields and Waves in Solids, Wiley, New York, 1973.
[55] J. Chen, X. Xu, J. Zhou, B. Li, Interfacial thermal resistance: Past, present, and future, Rev. Modern Phys. 94 (2) (2022) 025002, http://dx.doi.org/10.1103/RevModPhys.94.025002.
[56] T. Fang, X. Li, C. Hu, Q. Zhang, J. Yang, W. Zhang, X. Zhao, D.J. Singh, T. Zhu, Complex band structures and lattice dynamics of Bi2Te3-based compounds and solid solutions, Adv. Funct. Mater. 29 (28) (2019) 1900677, http://dx.doi.org/10.1002/adfm.201900677.
[57] H.J. Goldsmid, The thermal conductivity of bismuth telluride, Proc. Phys. Soc. Sect. B 69 (2) (1956) 203–209, http://dx.doi.org/10.1088/0370-1301/69/2/310.
[58] B.-L. Huang, M. Kaviany, Ab initio and molecular dynamics predictions for electron and phonon transport in bismuth telluride, Phys. Rev. B 77 (12) (2008) 125209, http://dx.doi.org/10.1103/PhysRevB.77.125209.
[59] A. Jena, S.-C. Lee, S. Bhattacharjee, Tuning the lattice thermal conductivity in bismuth telluride via Cr alloying, Phys. Rev. Appl. 15 (6) (2021) 064023, http://dx.doi.org/10.1103/PhysRevApplied.15.064023.
[60] C.B. Satterthwaite, R.W. Ure, Electrical and thermal properties of Bi2Te3, Phys. Rev. 108 (5) (1957) 1164–1170, http://dx.doi.org/10.1103/PhysRev.108.1164.
[61] Z. Zhang, Y. Guo, M. Bescond, J. Chen, M. Nomura, S. Volz, Coherent thermal transport in nano-phononic crystals: An overview, APL Mater. 9 (8) (2021) 081102, http://dx.doi.org/10.1063/5.0059024.
[62] S. Hu, M. An, N. Yang, B. Li, Manipulating the temperature dependence of the thermal conductivity of graphene phononic crystal, Nanotechnology 27 (26) (2016) 265702, http://dx.doi.org/10.1088/0957-4484/27/26/265702.
[63] Y. Zhang, D. Ma, Y. Zang, X. Wang, N. Yang, A modified theoretical model to accurately account for interfacial roughness in predicting the interfacial thermal conductance, Front. Energy Res. 6 (2018) http://dx.doi.org/10.3389/fenrg.2018.00048.
[64] S. Shan, Z. Zhang, S. Volz, J. Chen, Phonon mode at interface and its impact on interfacial thermal transport, J. Phys.: Condens. Matter. 36 (42) (2024) 423001, http://dx.doi.org/10.1088/1361-648X/ad5fd7.
[65] K. Khot, B. Xiao, Z. Han, Z. Guo, Z. Xiong, X. Ruan, Phonon local non-equilibrium at Al/Si interface from machine learning molecular dynamics, J. Appl. Phys. 137 (11) (2025) 115301, http://dx.doi.org/10.1063/5.0243641.
[66] J. Xu, Y. Guo, Uncovering the roughness effect on inelastic phonon scattering and thermal conductance at interface via spectral energy exchange, Int. J. Heat Mass Transfer 250 (2025) 127295, http://dx.doi.org/10.1016/j.ijheatmasstransfer.2025.127295.
[67] B. Qiu, X. Ruan, Molecular dynamics simulations of lattice thermal conductivity of bismuth telluride using two-body interatomic potentials, Phys. Rev. B 80 (16) (2009) 165203, http://dx.doi.org/10.1103/PhysRevB.80.165203.
[68] B. Qiu, X. Ruan, Thermal conductivity prediction and analysis of few-quintuple Bi2Te3 thin films: A molecular dynamics study, Appl. Phys. Lett. 97 (18) (2010) 183107, http://dx.doi.org/10.1063/1.3514252.
[69] X. Wang, X. Wu, P. Ying, Z. Fan, H. Sun, Interface phonon modes governing the ideal limit of thermal transport across diamond/cubic boron nitride interfaces, 2025, http://dx.doi.org/10.48550/arXiv.2504.18473, arXiv preprint.
[70] B. Liu, V.I. Khvesyuk, Analytical model for thermal boundary conductance based on elastic wave theory, Int. J. Heat Mass Transfer 159 (2020) 120117, http://dx.doi.org/10.1016/j.ijheatmasstransfer.2020.120117.
[71] B. Liu, M. Wang, Interfacial thermal transport driven by phonon wave behaviors and its tunability in GaN-on-diamond devices, Int. J. Heat Mass Transfer 229 (2024) 125700, http://dx.doi.org/10.1016/j.ijheatmasstransfer.2024.125700.
[72] Y. Guo, Z. Zhang, M. Bescond, S. Xiong, M. Nomura, S. Volz, Anharmonic phonon-phonon scattering at the interface between two solids by nonequilibrium Green's function formalism, Phys. Rev. B 103 (17) (2021) 174306, http://dx.doi.org/10.1103/PhysRevB.103.174306.
[73] Z.-Z. Yu, G.-H. Xiong, L.-F. Zhang, A brief review of thermal transport in mesoscopic systems from nonequilibrium Green's function approach, Front. Phys. 16 (4) (2021) 43201, http://dx.doi.org/10.1007/s11467-021-1051-3.